INL/EXT-21-64275 Rev. 0

August 2021

Mesoscale simulations to inform microstructure-based pulverization criterion in high-burnup UO_2

Larry Aagesen
Sudipta Biswas
Wen Jiang
David Andersson
Michael Cooper
Christopher Matthews

INL/EXT-21-64275 Rev. 0

Mesoscale simulations to inform microstructure-based pulverization criterion in high-burnup UO_2

Larry Aagesen
Sudipta Biswas
Wen Jiang
*David Andersson**
*Michael Cooper**
*Christopher Matthews**

August 2021

Idaho National Laboratory
Computational Mechanics and Materials Department
Idaho Falls, Idaho 83415

*** Los Alamos National Laboratory**
Materials Science and Technology Division
Los Alamos, NM 87545

Prepared for the
U.S. Department of Energy
Office of Nuclear Energy
Under U.S. Department of Energy-Idaho Operations Office
Contract DE-AC07-99ID13727

ABSTRACT

To improve the economics of commercial nuclear power production, utilities are seeking to increase the allowable burnup limit of UO_2 fuel. One of the main factors that contributes to the current burnup limit of 62 GWd/MTU in commercial light-water reactors (LWRs) is the risk of fine fragmentation or pulverization during a loss of coolant accident (LOCA). Pulverization primarily occurs at high burnups, especially when the high-burnup structure (HBS) has formed. To allow the industry to pursue increased burnup and develop mitigation strategies, it is essential to have improved capability to predict the onset of pulverization. However, the mechanism of pulverization is not well understood, and the existing predictive capabilities implemented in the BISON fuel performance code are empirical in nature.

In this report, mesoscale simulations are used to improve understanding of the formation mechanism of the HBS and how it responds during a LOCA transient, and inform development of a BISON pulverization criterion. A phase-field model was used to simulate the evolution of bubble pressure as a result of HBS formation. The simulations showed that gas atoms diffuse from grain interiors to the new grain boundaries created during HBS formation and diffuse rapidly along these grain boundaries to reach existing bubbles. This causes an increase in bubble pressure in existing bubbles, leading to bubble growth during steady-state operation. To simulate the response of HBS bubbles to a LOCA transient, a newly developed phase-field model was used; in agreement with preliminary results from Fiscal Year 2020, bubble size did not change significantly during the duration of the transient. A phase-field fracture model was used to study fragmentation patterns in the HBS. Phase-field fracture simulations were used to determine a pulverization criterion for BISON. A function for the critical pressure for pulverization to occur was fit to data from the phase-field fracture simulations, and this function was implemented as a material property in BISON. For comparison, an analytical criterion for pulverization was developed and implemented within the same material property.

CONTENTS

FIGURES

TABLES

1 INTRODUCTION

In order to improve the economics of commercial nuclear energy production, U.S. fuel vendors and utilities are seeking to increase the burnup limit of pellet-form UO_2 fuel for commercial light-water reactors (LWRs) from 62 GWd/MTU to as high as 75 GWd/MTU [1]. To gain approval for such an increase, vendors must demonstrate that fuel rods retain their safety aspects in the event of design-basis accidents. One significant challenge in increasing the burnup limit is to demonstrate safety in the case of a loss-of-coolant accident (LOCA). During a LOCA, fuel with higher burnup can fragment into very small pieces (a process sometimes referred to as pulverization) [2, 3]. In the event of a cladding rupture during the LOCA, these small fragments (with diameters of less than 100 μm [4]) could redistribute within the fuel rod or escape to the coolant in the event of a cladding burst. To allow LWR fuel to be licensed to higher burnups, the cause of this pulverization phenomenon must be better understood and mitigation strategies must be developed.

Although the cause of pulverization is not fully understood, it has been linked with the formation of the high-burnup structure (HBS) in UO_2 [4]. The formation of the HBS is itself not well understood, but it results in two main changes in the fuel microstructure. The first is the formation of a finer grain structure through a process of recrystalliation or polygonization [5]. This results in a decrease from typical as-fabricated grain sizes of 5–10 μm to much smaller sizes of 100–300 nm. At the same time, larger fission gas bubbles form with diameters on the order of 1 μm, with many of the new, smaller grains intersecting each bubble. These larger bubbles are believed to be significantly overpressurized with fission gases relative to the equilibrium pressure [6]. At the same time, fission gas is depleted in the fuel matrix surrounding the bubbles [7].

Although pulverization has sometimes been observed in regions where HBS formation is not fully complete [4], based on the more consistent observations of pulverization in the presence of the HBS, we focus here on pulverization in the presence of a fully formed HBS. During a LOCA transient, a rapid increase in temperature occurs, causing an increase in pressure in the already overpressurized bubbles in the HBS region. It has been hypothesized that this rapid increase in pressure induces stresses in the surrounding matrix that are high enough to cause fracture along the grain or subgrain boundaries that intersect the large bubbles in the HBS region, leading to fine fragmentation. Although the mechanism of pulverization is not fully understood, because of its importance to fuel performance, an empirical criterion for pulverization has been implemented in Idaho National Laboratory's (INL's) fuel performance code, BISON, based on experimental data [4]. However, to provide a predictive capability outside the conditions in which these experiments were conducted, a mechanistic criterion for pulverization that accounts for the microstructure of the fuel is desired.

In this report, mesoscale simulations aimed at informing a mechanistic criterion for pulverization are described. The outline of the report is as follows. In Section 2, a phase-field model based on a grand potential functional is used to study the formation and evolution of the HBS and the evolution of bubbles and gas bubble pressure following the formation of the HBS. The model used is a phase-field model that can account for multiple grains of the fuel matrix, the bubble phase, and the restructuring of the grains that results in decreasing grain size. The model has been parameterized using atomistic calculations, including the diffusivities of defect species. The model was used to simulate the evolution of bubbles just after the formation of the HBS. These simulations showed that gas atoms that are initially supersaturated in the fuel grains are transported to the newly formed grain boundaries. These grain boundaries then rapidly transport some gas atoms to existing bubbles, causing growth of existing bubbles, while other gas atoms form new bubbles. The bubble pressure in the existing bubbles increases, leading to bubble growth.

In Section 3, a phase-field model is employed to study the response of the gas bubbles to a LOCA transient, as well as steady-state growth. A preliminary version of the model was described in Fiscal Year (FY) 2020. This model is based on the Kim-Kim-Suzuki phase field model. It accounts for the gas bubble pressure and the bubble-matrix surface tension on the stress state of the surrounding fuel. The current version of the model only allows consideration of a single grain of the fuel matrix, unlike the model used in Section 2; however, the model may be extended to consider multiple grains in the future. In this report, the model's

behavior is verified through comparison with the analytical solution for the stress state in the fuel matrix surrounding underpressurized, overpressurized, and equilibrium bubbles. The model is used to simulate steady-state growth in bubbles in the HBS region, as well as the response of bubbles to LOCA transients. In agreement with preliminary results from FY-20, the bubbles do not change size significantly during the duration of a LOCA transient. This simplifies phase-field fracture simulations described in the next section because the fracture model does not need to simultaneously account for bubble size change.

Phase-field fracture simulations are used to understand the fracture behavior during LOCA transients in Section 4. The model employed accounts for the pressure in the gas bubble, which propagates along the opening crack face. The model is used to demonstrate the importance of multi-bubble interactions, suggesting that such multi-bubble interactions should be considered when determining a pulverization criterion. The model is capable of simulating fracture in regions where the HBS is only partially formed, using microstructures generated from the model of Section 2 as input. Simulations using this model with periodic boundary conditions to account for multi-bubble interactions are used to generate data for a mechanistic model of pulverization for BISON.

The implementation of the mechanistic model of pulverization in BISON is described in Section 5. The model calculates the current pressure of the most frequently observed bubble size in the HBS region. It calculates the critical pressure for pulverization using either an analytical model or a model based on a fit to the phase-field fracture data described in Section 4. Pulverization is deemed to occur if the current bubble pressure is greater than the critical pressure. Finally, in Section 6, the main conclusions are highlighted and directions for future work are suggested.

2 HBS FORMATION AND BUBBLE GROWTH

In UO_2 fuel, regions exposed to high burnup and low temperatures exhibit a fine-grained microstructure with large bubbles known as high burnup structure (HBS). The key characteristics of the region include a) accumulation of dislocations leading to creation of large dislocation networks, b) recrystallization of new defect free sub-grains, c) depletion of intra-granular fission gas concentration, and d) formation of large spherical inter-granular bubbles [5]. Understanding the HBS formation and its impact on the thermo-mechanical properties of the nuclear fuel is very important to evaluate the performance of the fuel. This region is also known to be prone to fragmentation and even pulverization, especially during LOCA scenarios.

Pulverization has been noticed in partially and fully recrystallized high-burnup regions. Although the reason behind pulverization is not fully understood, it has been attributed to fine grained structures with high-pressure bubbles. With recrystallization, GB density in the fuel increases, which weakens the fracture strength leading to fuel fragmentation. In order to predict the fragmentation criteria, it is paramount to appropriately predict the HBS formation and associated bubble growth and pressure evolution.

The phase-field modeling approach is utilized to investigate the mechanisms facilitating the creation of such a structure. In previous years, a recrystallization model was developed to capture the HBS formation and the contribution of various defect species leading to creation of larger bubbles as observed in the HBS structures [8, 9]. It was demonstrated that the model can capture concurrent recrystallization and associated bubble evolution in nuclear fuels. It was observed that bubble growth accelerates after completion of the HBS formation rather than during. This year the primary focus has been on parameterizing the model with appropriate LWR conditions and utilizing athermal irradiation-enhanced material properties to improve the predictability of the model. Additionally, associated bubble pressure is calculated from these simulations to provide input for initial bubble pressure for LOCA transient simulations.

In this section, we provide a brief account of the grand potential-based bubble evolution model with details about the parameterization for LWR conditions. We also summarize the material properties and irradiation conditions available in literature that are used in the model. The model accounts for existing fission gas bubbles and concurrently tracks the concentration of defects, such as vacancies and gas atoms, leading to further bubble growth and pressure increase. Additionally, it considers the role of defect sources, recombination of defects, various diffusion mechanisms, and activation paths contributing to formation of new bubbles and coalescence of smaller bubbles into the larger ones. The model predicts growth of existing bubbles and formation of new intergranular as well as intra-granular bubbles. Some of these bubbles physically appear at a lower length scale which presents numerical challenges for the mesoscale simulations. We briefly talk about the challenges faced, mitigation strategies adopted, and future improvements to be made.

2.1 Phase-field Model Formulation

The HBS bubble growth model presented in this section is formulated based on the grand-potential-based multi-order multi-component phase-field model. The model is capable of capturing the evolution of multiple phases, grains, and chemical species concurrently. It has previously been applied to model phase separation, solidification, and sintering of complex alloy systems [10, 11, 12, 13]. Recently, Aagesen et al. [14, 15] applied the model to evaluate the bubble evolution in various nuclear materials. In FY-20, the model was combined with the grain nucleation model to simulate the recrystallization and porosity evolution that produces the key characteristics of the HBS. Here, we primarily focus on utilizing the same model for bubble growth and associated pressure buildup in bubbles within fine grained HBS.

In this model, the microstructure is considered to have two significant and distinguishable crystallographic features: solid matrix and bubble. Within the matrix, multiple grains are represented with different order parameters, $\eta_{m0}, \eta_{m1}, \ldots \eta_{mi}, \ldots \eta_{mn}$, and the bubble is represented by a single order parameter, η_b. Additionally, local concentration of various defect species such as vacancies and fission gases are represented

as chemical components; the number density of which are presented with ρ_v and ρ_g, respectively.

2.1.1 Grand potential functional

The evolution equations for the microstructure are derived from the total grand potential Ω of the system. It is obtained from local grand potential density expressed in terms of the free energy density of the system as

$$\Omega = \int_V \left[f_{bulk}\left(\eta_{mi}, \eta_b\right) + f_d(\eta_{mi}) + f_{gr}(\eta_{mi}, \eta_b) + h_b\omega_b + h_m\omega_m \right] dV \,. \tag{1}$$

Here, the bulk free energy density term (f_{bulk}) ensures that a minimum in the free energy exists within the interior of each grain and contributes to the interfacial energies between different phases/grains. The gradient energy term (f_{gr}) penalizes the gradients of the order parameters representing each grain/phase and also contributes to the interfacial energies between different grains/phases. For capturing recrystallization, the dislocation energy density (f_d) for the deformation energy density due to dislocation pile up is taken into account. For the current bubble growth model, the contribution of (f_d) is set to zero. Finally, the fourth and fifth terms add the appropriate grand potential density for each phase.

The bulk free energy density is defined as

$$f_{bulk} = \alpha \left[\left(\frac{\eta_b^4}{4} - \frac{\eta_b^2}{2} \right) + \sum_{i=1}^{n_m} \left(\frac{\eta_{mi}^4}{4} - \frac{\eta_{mi}^2}{2} \right) + \left(\frac{\gamma_{bm}}{2}\eta_b^2 \sum_i \eta_{mi}^2 + \sum_i^{n_m} \sum_{i\neq j}^{n_m} \frac{\gamma_{mm}}{2}\eta_{mi}^2\eta_{mj}^2 \right) + \frac{1}{4} \right] \tag{2}$$

where m and b represent the matrix and bubble phases, i and j are indices for the grains, n_m is the total number of grains, and α is a constant free energy barrier coefficient. γ_{mb} and γ_{mm} are constant parameters that allow adjustment of interfacial energies between phases and grains. The model assumes isotropic interfacial properties without consideration of inclination or misorientation dependence. ($\frac{\alpha}{4}$) is added to make the homogeneous free energy density equal to 0 within grain interiors. The gradient free energy density is expressed as

$$f_{gr} = \frac{\kappa}{2} \left(|\eta_b|^2 + \sum_{i=1}^{n_m} |\nabla\eta_{mi}|^2 \right) , \tag{3}$$

with κ being the gradient energy coefficient.

In Equation 1, ω_m and ω_b are the local grand potential density of matrix and bubbles phases, and h_m and h_b are the switching functions used for interpolating the grand potential density between the phases. For the matrix and bubble phases, the switching functions are

$$h_m = \frac{\sum_{i=1}^{n_m} \eta_{mi}^2}{\eta_b^2 + \sum_{i=1}^{n_m} \eta_{mi}^2} \,, \tag{4}$$

and

$$h_b = \frac{\eta_b^2}{\eta_b^2 + \sum_{i=1}^{n_m} \eta_{mi}^2} \,, \tag{5}$$

respectively. The grand potential density for each phase is given by

$$\omega_m = f_m - \mu_g\rho_g - \mu_v\rho_v \,, \tag{6}$$

and

$$\omega_b = f_b - \mu_g\rho_g - \mu_v\rho_v \,, \tag{7}$$

where f_m and f_b are the Helmholtz free energies of each phase, and μ_g and μ_v are the chemical potentials of the gas atoms and vacancies.

2.1.2 Chemical free energy density

Assuming the chemical energy of the matrix follows the ideal solution model, the Helmholtz free energy density is described as

$$f_{m,ideal} = \frac{1}{V_m}\Big\{RT\left[c_v \ln c_v + (1-c_v)\ln(1-c_v)\right] + N_A E_v^f c_v \\ + RT\left[c_g \ln c_g + (1-c_g)\ln(1-c_g)\right] + N_A E_g^f c_g\Big\}, \tag{8}$$

where R is the ideal gas constant, V_m is the molar volume such that $V_m = V_a N_A$, N_A is Avogadro's number, V_a is the atomic volume, E_v^f is the formation energy of a U vacancy, E_g^f is the formation energy of a gas (Xe) atom on a U lattice site, and T is the temperature. c_v and c_g represents the concentration of vacancies and gas atoms in the matrix. To improve numerical performance, $f_{m,ideal}$ is approximated with a parabolic function

$$f_m = \frac{1}{2}k_v^m(c_v - c_v^{m,eq})^2 + \frac{1}{2}k_g^m(c_g - c_g^{m,eq})^2, \tag{9}$$

where k_v^m and k_g^m are the curvatures of the parabolas and $c_v^{m,eq}$, and $c_g^{m,eq}$ are the equilibrium concentration of vacancies and gas atoms in the UO_2 matrix. The equilibrium concentrations are determined from the formation energies and temperature using $c_v^{m,eq} = \exp(-E_v^f/k_B T)$ and $c_g^{m,eq} = \exp(-E_g^f/k_B T)$, where k_B is the Boltzmann's constant. The curvatures of the parabolas are set by assuming that when the vacancy composition, c_v, is equal to the steady-state vacancy composition during reactor operation, c_v^0, the chemical potential determined from the parabolic approximation is equal to the chemical potential of the ideal solution model as described in [14]. Since $\mu = \frac{\partial f}{\partial \rho} = \frac{\partial f}{\partial c}\frac{\partial c}{\partial \rho} = V_a \frac{\partial f}{\partial c}$,

$$V_a \frac{\partial f_m}{\partial c_v}\bigg|_{c_v^0} = V_a \frac{\partial f_{m,ideal}}{\partial c_v}\bigg|_{c_v^0} \tag{10}$$

This leads to an expression for k_v^m,

$$k_v^m = \frac{1}{\left(c_v^0 - c_v^{m,eq}\right)}\left[\frac{RT}{V_m}\left[\ln c_v^0 - \ln(1-c_v^0)\right] + \frac{N_A E_v^f}{V_m}\right] \tag{11}$$

Here, c_v^0 is chosen based on cluster dynamics simulations, as described further in Section 2.1.6. For $c_v^0 = 0.01$, k_v^m varies linearly with temperature such that $k_v^m = 7335\,\mathrm{eV/nm^3} - 0.9682\,T\,\mathrm{eV/nm^3/K}$. Similarly, for the the gas atoms, the parabola curvature is estimated by equating the chemical potentials obtained from the ideal solution model to the value obtained from the parabolic approximations for the matrix gas concentration prior to HBS formation. Following Equation 11, for $c_g^0 = 0.02$ this yields $k_g^m = 3667.5\,\mathrm{eV/nm^3} - 0.41\,T\,\mathrm{eV/nm^3/K}$. This value of c_g^0 is chosen based on the peak of intragranular Xe concentration, which occurs at the onset of HBS formation, as discussed further in Section 2.1.4.

The bulk chemical free energy density of the gas bubble phase, f_b, is determined by considering the gas phase to be a mixture of U-site vacancies and Xe atoms as described in [14]. It is assumed that the van der Waals gas equation of state applies to Xe [16], in which the gas atoms are assumed to have a hard-sphere exclusion volume characterized by the parameter b, and we neglect long-range interactions due to the high density of gas in the bubbles. For Xe, $b_g = 0.085$ nm^3/atom [16]. With these assumptions, the Helmholtz free energy density of the gas is [17]

$$f_{b,vdW} = n_g kT\left[\ln\left(\frac{1}{n_Q\left(\frac{1}{n_g} - b_g\right)}\right) - 1\right] + f_0\,, \tag{12}$$

where n_g is the number density of gas atoms, $n_Q = \left(\frac{2\pi m k_B T}{h^2}\right)^{3/2}$ is the quantum concentration, m is the mass of a Xe atom, h is the Planck constant, and f_0 is the offset to ensure that the solid and gas free energies are measured relative to the same reference state. n_g can be expressed in terms of the model variables using $n_g = c_g n_U$, where $n_U = 1/V_a$ is the number density of U atoms in the UO_2 lattice, such that $c_v + c_g = 1$ is maintained. f_0 is determined by setting the minima of the gas and solid phase chemical free energies to be equal. By solving the system for the temperature range $700 \leq \mathrm{T} \leq 1300$, f_0 is fitted to be $f_0 = 4.9 \times 10^{-3}\, T\, \mathrm{eV/nm^3/K} - 0.58\, \mathrm{eV/nm^3}$.

To simplify the numerical calculations, the Helmholtz free energy of the gas phase is also approximated utilizing a parabolic fit

$$f_b = \frac{1}{2}k_v^b(c_v - c_v^{b,eq})^2 + \frac{1}{2}k_g^b(c_g - c_g^{b,eq})^2 \tag{13}$$

The minimum of the parabolic free energy was set to occur at the minimum of the Van der Waals free energy. Because composition in the gas bubbles will generally not deviate far from the minimum of the free energy, k_v^b and k_g^b are set by assuming $k_v^b = k_g^b$ and fitting to $f_{b,vdW}$ in the range $0.42 < c_g < 0.47$. k_v^b value can be approximated as $k_v^b = 0.2328\, T\, \mathrm{eV/nm^3/K} - 30.723\, \mathrm{eV/nm^3}$.

Figure 1 provides the free energy density landscapes for both the species corresponding to temperatures of 1000 K and 1200 K.

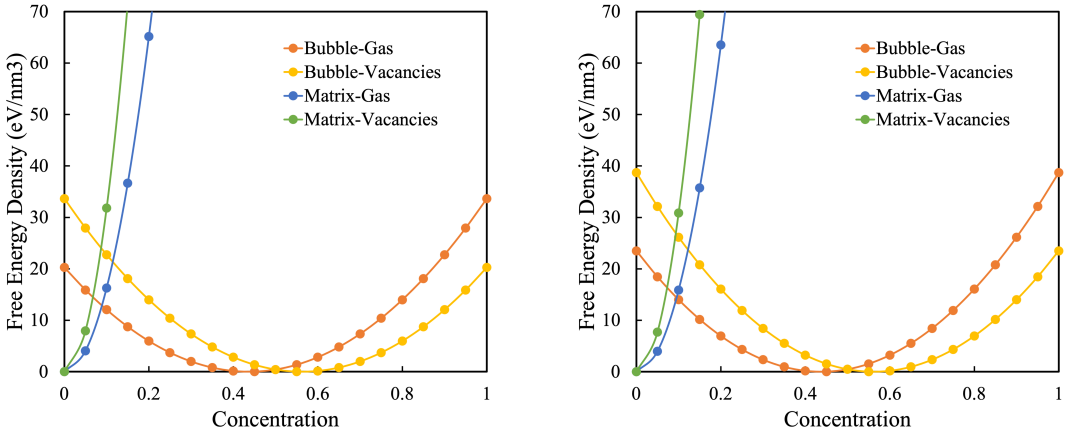

Figure 1: Free energy density plots for vacancies and gas atoms at temperatures 1000 K (a), and 1200 K (b).

2.1.3 Governing equations

The evolution of the order parameters is captured using the Allen-Cahn equations. From the grand potential functional of Equation (1), the evolution equations of the order parameters are derived as

$$\begin{aligned} \frac{\partial \eta_{mi}}{\partial t} &= -L\frac{\delta \Omega}{\delta \eta_{mi}} \\ \frac{\partial \eta_b}{\partial t} &= -L\frac{\delta \Omega}{\delta \eta_b} \end{aligned} \tag{14}$$

where L is the kinetic mobility of the order parameters, and $\frac{\delta \Omega}{\delta \eta_{mi}}$ and $\frac{\delta \Omega}{\delta \eta_b}$ are the variational derivatives of Ω with respect to order parameter η_{mi} and η_b, respectively.

To evolve the gas and vacancy concentrations, it is more convenient to write the evolution equations in terms of chemical potentials μ_v and μ_g and use the chemical potentials as the field variables rather than the densities. To enable this, the grand potentials in each phase, Equations (6) - (7), must be expressed in terms of μ_v and μ_g. For the matrix phase, the relation $\mu_g = V_a \frac{\partial f_{m,chem}}{\partial c_g} = V_a k_g^m (c_g - c_g^{m,eq})$ can be re-arranged to yield

$$c_g = \frac{\mu_g}{V_a k_g^m} + c_g^{m,eq} . \tag{15}$$

Similarly, for the vacancies

$$c_v = \frac{\mu_v}{V_a k_v^m} + c_v^{m,eq} . \tag{16}$$

Equations (15) – (16) can be used in conjunction with the relations $\rho_g = \frac{c_g}{V_a}$, $\rho_v = \frac{c_v}{V_a}$ and Equations (6) and (9) to obtain the grand potential density as a function of the chemical potentials rather than the concentrations

$$\omega_m = -\frac{1}{2}\frac{\mu_v^2}{V_a^2 k_v^m} - \frac{\mu_v}{V_a} c_v^{m,eq} - \frac{1}{2}\frac{\mu_g^2}{V_a^2 k_g^m} - \frac{\mu_g}{V_a} c_g^{m,eq} . \tag{17}$$

Similarly, the grand potential density of the bubble phase can be expressed as

$$\omega_b = -\frac{1}{2}\frac{\mu_v^2}{V_a^2 k_v^b} - \frac{\mu_v}{V_a} c_v^{b,eq} - \frac{1}{2}\frac{\mu_g^2}{V_a^2 k_g^b} - \frac{\mu_g}{V_a} c_g^{b,eq} . \tag{18}$$

The evolution equations for μ_g and μ_v are

$$\frac{\partial \mu_g}{\partial t} = \frac{1}{\chi_g}\left[\nabla \cdot \left(D_g \chi_g \nabla \mu_g\right) + s_g - \frac{\partial \rho_g}{\partial \eta_b}\frac{\partial \eta_b}{\partial t} - \sum_{i=1}^{n_m} \frac{\partial \rho_g}{\partial \eta_{mi}}\frac{\partial \eta_{mi}}{\partial t}\right] \tag{19}$$

$$\frac{\partial \mu_v}{\partial t} = \frac{1}{\chi_v}\left[\nabla \cdot \left(D_v \chi_v \nabla \mu_v\right) + s_v - D_v k_v \rho_v - \frac{\partial \rho_v}{\partial \eta_b}\frac{\partial \eta_b}{\partial t} - \sum_{\alpha}\sum_{i=1}^{p_\alpha} \frac{\partial \rho_v}{\partial \eta_{\alpha i}}\frac{\partial \eta_{\alpha i}}{\partial t}\right] \tag{20}$$

where D_g and D_v are the diffusion coefficients, and s_g and s_v are the source terms for production of Xe atoms and U site vacancies. χ_g and χ_v are the susceptibilities defined as

$$\chi_g = h_m \frac{1}{V_a^2 k_g^m} + h_b \frac{1}{V_a^2 k_g^b} \tag{21}$$

$$\chi_v = h_m \frac{1}{V_a^2 k_v^m} + h_b \frac{1}{V_a^2 k_v^b} \tag{22}$$

2.1.4 Diffusion coefficients

Diffusion of U-vacancies and U-substitutional Xe gas atoms play a pivotal role dictating the bubble growth and pressure increase. For temperatures, at which HBS is dominant, the diffusion is usually athermal and driven by irradiation. There is very limited data regarding the diffusion coefficients for vacancies and gas atoms at low temperatures. Experimentally, effect of irradiation on the gas atoms is determined based on the gas release behavior of UO_2. Davies and Long [18] reported $D_g = 7.6 \times 10^{-10} \exp(-3.04/k_B T)$ m^2/s from their experimental study. Turnbull [19] demonstrated that diffusion behavior of Xe under irradiation is a complex phenomenon involving multiple rate controlling mechanisms. Above 1400^{o}C, they used the

same intrinsic diffusion values as calculated by Davies and Long [18]. For lower temperature, an irradiation enhanced diffusion coefficient of $D = 2 \times 10^{-40} F$ m^2/s is considered, where F is the neutron flux. Miekeley and Felix studied the Xe diffusion in stochiometric UO_2 during post irradiation annealing experiments. The average diffusivity reported for UO_2 is $D_0 \exp(-3.9/k_B T)$. Here, D_0 varies from 5×10^{-2} to 5.0 cm^2/s within the temperature range of 950 ^{o}C to 1700^{o}C. At 1200 K, this provides an approximate diffusivity value of 0.0258 nm^2/s. For the temperature range 600–1300^{o}C, different stochiometry and diffusion values are observed. The diffusivity in this case is $D_0 \exp(-1.7/k_B T)$, with D_0 varying from 1×10^{-8} to 1.0×10^{-4} cm^2/s. Matthews et al. [20] derived the diffusion values considering the mobilities of different Xe clusters. The diffusivity values obtained from the cluster dynamics simulations are fitted as,

$$D_g = D_1(T) + D_2(T, \dot{F}) + D_3(\dot{F}) \tag{23}$$

$$D_1(T) = \frac{2.22 \times 10^{-7} \exp(-3.26/k_B T)}{1 + 29.0 \exp(-1.84/k_B T)} \tag{24}$$

$$D_2(T, \dot{F}) = 2.82 \times 10^{-22} \exp(-2.0/k_B T)\sqrt{\dot{F}} \tag{25}$$

$$D_3(\dot{F}) = 8.5 \times 10^{-40} \dot{F} \tag{26}$$

where D_g is in unit of m^2/s. For typical LWR fission rate density of 1.09 $\times10^{19}$ fissions/m^3-s and 1200 K temperature, the gas diffusion value is 1.75×10^{-20} m^2/s or 0.0175 nm^2/s. For 1100 K, 1000 K, 900 K the values are 1.02 $\times10^{-2}$, 9.35 $\times10^{-3}$, 9.27 $\times10^{-3}$ nm^2/s, respectively. Below 900 K, athermal diffusion dominates, and the diffusivity value of 9.27 $\times10^{-3}$ nm^2/s persists. For the phase field simulations, this D_g value is used as the bulk diffusion coefficient for the gas atoms in the matrix. Enhanced diffusion coefficients are used within the bubbles, along the grain boundaries and the bubble surfaces. Figure 2a compares the cluster-dynamics data to the experimental values.

For capturing the gas concentration in matrix and bubbles, gas evolution in HBS has been studied experimentally using the electron probe microanalysis (EPMA) technique. Spino [21] documented the Xe created and retained in the matrix as burnup increases. Lassman also predicted Xe fraction evolution with burnup. Figure 2b reproduces and compares the evolution of the Xe concentration with burnup predicted by different researchers. The Xe-concentration in the matrix prior to HBS formation is 0.02 atomic fraction and the steady-state concentration is observed to be 0.005. These values can be utilized to fit the parabola curvature of the chemical free energy corresponding to gas atoms. This concentration plot is also used to select appropriate gas supersaturation values in the matrix while setting up the initial conditions for the simulations.

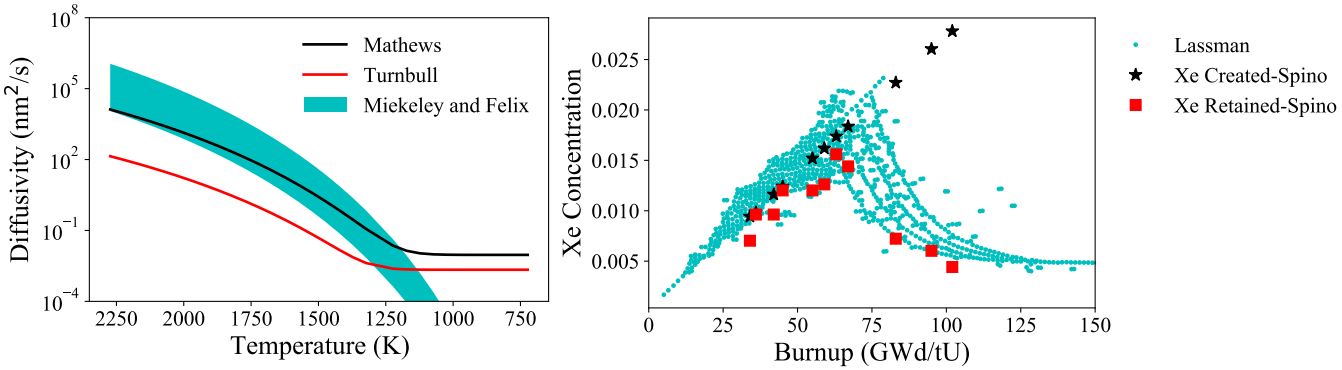

Figure 2: (a) Diffusivity of Xe atoms in UO_2. (b) Experimentally measured intragranular Xe concentration in UO_2 fuel matrix as a function of burnup.

The diffusion coefficients for vacancies and other defects in UO_2 determines the self diffusion of UO_2. The diffusion values obtained in the literature widely vary. Here, we present an account of the values available. Matzke [22] studied the irradiation enhanced diffusion of U in UO_2. The diffusion coefficient is observed to be independent of temperature and varies linearly with the fission rate, $D_U = 1.2 \times 10^{-29} \dot{F}$ cm^2/s. For the fission rate density of 1.09 $\times 10^{19}$ fissions/m^3-s, $D_U = 0.0131$ nm^2/s. Assuming the uranium diffusion is driven by the vacancies only, the vacancy diffusivity can be estimated using $D_v = D_U / \alpha_v c_{v0}$, where $\alpha_v = 0.781$ is the correlation factor for vacancies. Thus the vacancy diffusion coefficient becomes 1.677 nm^2/s for $c_{v0} = 0.01$ and 2.1 nm^2/s for $c_{v0} = 0.008$. Later, Matzke [23] considered the effect of temperature on the uranium self diffusion and reported a diffusivity of 0.65 $\exp(-5.6/k_B T) cm^2/s$ for $T < 1500^o C$. In the same work, effects of irradiation on the diffusion of vacancies and interstitials were studied. The reported values are $D_{v_U} = 2 \times 10^{-3} \exp(-2.4/k_B T)$ cm^2/s and $D_{U_i} = 1 \times 10^{-1} \exp(-2.0/k_B T)$ cm^2/s. This indicates that uranium interstitials are more mobile than the vacancies. At 1200 K, this yields the vacancy diffusion value of 16.653 nm^2/s. However, the diffusion coefficients obtained from the cluster dynamics simulations are different from the experimental values. Figure 3 shows the diffusivities and concentrations of various defect species. Since the diffusivity values vary by several order of magnitude between different defect clusters and the model currently does not have the capability of directly utilizing these data, we use experimental diffusion coefficients observed by Matzke and set the lower limit on the diffusivity at the irradiation enhanced value of 1.677 nm^2/s. The steady-state vacancy concentration in the matrix is considered as 0.01 atomic fraction.

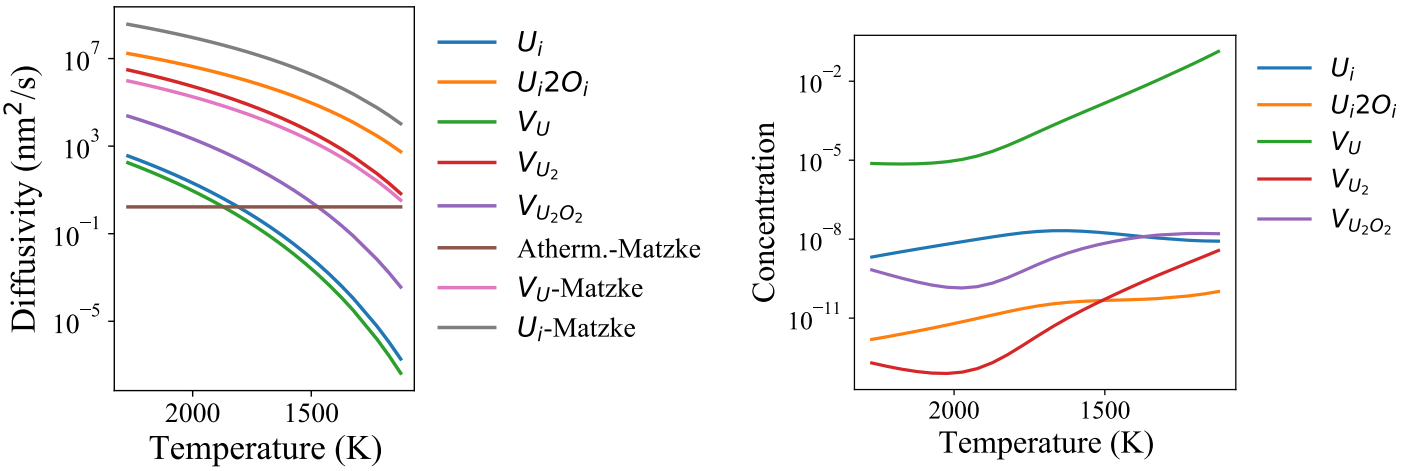

(a) (b)

Figure 3: Diffusion coefficients (a) and concentration (b) of various defects

Furthermore, enhanced diffusion along the GBs and bubble surfaces is considered to facilitate the species transport in HBS. The diffusion of both vacancies and gas atoms follow the following relation

$$D = D_m h_m + D_b h_b + 30 D_s \eta_b^2 (1 - \eta_b)^2 + 9 D_{gb} \sum_i \sum_{j \neq i} \eta_{mi}^2 \eta_{mj}^2 \tag{27}$$

where D_m is the bulk diffusion coefficient in the matrix, D_b is the diffusion coefficient within bubbles, D_s is the coefficient for surface diffusion, and D_{gb} is the coefficient of diffusion along grain boundaries. The prefactors for the diffusion along various interfaces are chosen such that, $\int_0^1 D_i f(\eta_i)\, d\eta_i = D_i$, where D_i denotes the diffusivity along the interface (i.e., D_s or D_{gb}). Equation 27 is used to incorporate the effect of different diffusion mechanisms in the model.

2.1.5 Interfacial properties

Here, we describe the interfacial parameterization of the model for HBS formation in UO_2 at 1200 K. The energy density, length, and time scales used for non-dimensionalizing the model are 1 eV/nm^3, 1 nm, and 1 sec, respectively. In general, the grain boundary energy of UO_2 is considered to be $\sigma_{mm} = 1.5$ J/m^2 or 9.363 eV/nm^2. The interfacial energy between the matrix and gas bubble phase is considered to be same as the grain boundary energy, $\sigma_{mb} = \sigma_{mm}$. This indicates a dihedral angle of 120° between the bubbles and the grain boundaries. The interfacial properties are calculated assuming interface thickness $l_{int} = 10$ nm. The free energy coefficients are obtained as [24]

$$\alpha = \frac{6\sigma_{mm}}{l_{int}}\,, \tag{28}$$

and

$$\kappa = \frac{3}{4}\sigma_{mm} l_{int}\,. \tag{29}$$

The kinetic mobility is obtained as

$$L = \frac{4M_{GB}}{3l_{int}}, \tag{30}$$

where M_{GB} is the grain boundary mobility:

$$M_{GB} = M_0 \exp\left(-\frac{Q}{k_B T}\right)\,, \tag{31}$$

where $M_0 = 9.21 \times 10^{-9}$ m^4/Js, $Q = 3.01$ eV [25], and k_B is the Boltzmann constant. Table 1 summarizes the model parameters with sample values for 1200 K.

2.1.6 Defect production and annihilation

The source term for the gas atoms is given by $s_g = s_{g0} h_m$, where S_{g0} is the constant Xe production rate, and h_m is the switching function which takes a value of 1 within the matrix and 0 inside the gas bubbles. The switching function limits the Xe production to the grains. The constant Xe production rate is computed from the fission rate such that $s_{g0} = Y_{Xe}\dot{F}$; where $\dot{F}$ is the fission rate density, and Y_{Xe} is the fission yield of Xe. For typical LWR, $\dot{F}$ is estimated as $1.09{\times}10^{19}$ fission/(m^3-s), and Y_{Xe} is 0.2156. Thus, the production rate is $2.35{\times}10^{18}$ atoms/m^3-s or $2.35{\times}10^{-9}$ atoms/nm^3-s. The vacancy production rate s_v is set at $20s_g$ (i.e., 4.7 $\times 10^{-8}$ atoms/nm^3-s).

Since the current model does not track the interstitials, it ensures that the steady-state vacancy concentration is maintained in the domain by introducing a vacancy sink term. This captures the essence of the recombination of vacancies and interstitials and helps maintain the steady-state vacancy concentration in the matrix. The sink strength is obtained from the steady-state conditions away from the large bubbles. At the steady state, the phase-field variables, including the vacancy concentration and order parameters, remain constant over time such that $\frac{\partial \mu_g}{\partial t} = 0$ and $\frac{\partial \eta_{\alpha i}}{\partial t} = 0$. Additionally, the vacancy concentration away from the bubbles does not vary spatially, hence, $\nabla \mu_g = 0$. Substituting these values in Equation 20,

$$s_{v0} - D_v k_{v0} \rho_{v0} = 0 \tag{32}$$

$$k_{v0} = \frac{s_{v0}}{D_v \rho_{v0}} \text{ or } \frac{s_{v0} V_a}{D_v c_{v0}} \tag{33}$$

Parameter	Formulation	Value	Source
T		1200 K	
V_a		0.04092 nm^3	[26]
E_f^v		3 eV	[14]
E_f^g		3 eV	[14]
$c_{v/g}^{m,eq}$	$\exp\left(-\frac{E_v^f}{k_B T}\right)$	2.515×10^{-13}	Section 2.1.2
k_v^m	$7335\,\text{eV/nm}^3 - 0.9682\,T\,\text{eV/nm}^3\text{/K}$	6173.17 eV/nm^3	Section 2.1.2
k_g^m	$3667.5\,\text{eV/nm}^3 - 0.41\,T\,\text{eV/nm}^3\text{/K}$	3175.5 eV/nm^3	Section 2.1.2
$c_v^{b,eq}$		0.562	Section 2.1.2
$c_g^{b,eq}$		0.438	Section 2.1.2
$k_{v/g}^b$	$0.2328\,T\,\text{eV/nm}^3\text{/K} - 30.723\,\text{eV/nm}^3$	245 eV/nm^3	Section 2.1.2
l_{int}		10 nm	
σ_{mm}		1.5 J/m^2 or 9.363 eV/nm^2	
κ	$\frac{3}{4}\sigma_{mm} l_{int}$	1.125×10^{-8} J/m or 70.2 eV/nm	Section 2.1.5
α	$\frac{6\sigma_{mm}}{l_{int}}$	9×10^8 J/m^3 or 5.62 eV/nm^3	Section 2.1.5
f_0	$4.9 \times 10^{-3}\,T\,\text{eV/nm}^3\text{/K} - 0.58\,\text{eV/nm}^3$	5.316 eV/nm^3	Section 2.1.2
G		64.1 GPa	[27]
M_{GB}	$9.21 \times 10^{-9} \exp\left(-\frac{3.01}{k_B T}\right)$ m^4/Js	3.43×10^{-4} nm^4/eV/s	Section 2.1.5
L	$\frac{4M_{GB}}{3l_{int}}$	4.58×10^{-5} nm^3/eV/s	Section 2.1.5
S_{g0}	$Y_{Xe}\dot{F}$	2.35×10^{-9} atoms/nm^3-s	Section 2.1.6
S_{v0}	$20 S_{g0}$	4.7×10^{-8} atoms/nm^3-s	Section 2.1.6
k_v	$\frac{s_{v0} V_a}{D_v c_{v0}}$	$2.4 \times 10^{-7} \frac{1}{D_v}$ /nm^3-s	Section 2.1.6

Table 1: Parameters used for phase-field simulations of bubble evolution in HBS

The steady-state vacancy concentration considered in the simulation is 0.01 (this is only slightly higher than the values obtained from the cluster dynamics simulations). Hence, the constant sink strength is obtained as, $1.9223\times10^{-7}/D_v$ atoms/nm^3-s. For $c_{v0} = 0.008$; the sink strength becomes $2.4\times10^{-7}/D_v$. Similar to the source terms, the vacancy sink term is also limited to the fuel matrix such that $k_v = h_m k_{v0}$. The effect of the sink term on the bubble growth is presented in the following section. It is note worthy here that the net vacancy production rate remains constant in the simulation irrespective of the vacancy source terms. Hence, higher vacancy source has not been considered in the model.

2.1.7 Computational details

For implementation and numerical solultion of the current model, we utilize the open-source parallel MOOSE framework. It is a fully coupled, fully implicit finite element solver with adaptive time stepping and adaptive meshing capabilities. It utilizes the PETSc solver library and the vast finite element library from LibMesh. For the 2D simulations presented here, the finite element meshes are comprised of four-node quadrilateral elements (QUAD4). Meshes are generated with the internal MOOSE mesh generator and linear lagrange shape functions are used for all the nonlinear variables. The system of nonlinear equations is solved with the preconditioned Jacobian Free Newton-Krylov (PJFNK) [28] method. We employ the additive Schwarz method (ASM) for preconditioning and iterative LU factorization for sub-preconditioning. The simulations

are solved with a linear tolerance of 1×10^{-3}, nonlinear relative tolerance of 1×10^{-6}, and a nonlinear absolute tolerance of 1×10^{-8}. Automatic residual scaling is utilized to minimize any disparities in the residual norms of corresponding to different nonlinear variables. For the time integration, an implicit time integration scheme with second order backward differentiation formula (BDF2) is employed. Furthermore, adaptive meshing and time stepping schemes were used to reduce the computational cost. The mesh is refined around the interface and coarsened in the other areas. This is achieved by refining the mesh in regions of high curvature in the order parameter fields with the help of a gradient jump indicator scheme [29] within MOOSE. The element sizes vary between 6.25 nm to 50.0 nm with three levels of mesh refinement/coarsening. Further mesh refinement did not impact the microstructural evolution. This adaptive meshing scheme allows us to appropriately resolve the interface without significantly increasing the computational cost. Additionally, an iteration-based time adaptivity scheme is employed to increase the time step, based on the number of iterations required to solve the coupled equation system. The optimal iteration window of 6 ± 1 is adopted. Periodic boundary conditions are used to eliminate any boundary effect on the solution.

2.2 Results and Discussion

We have performed several 2D simulations to evaluate the defect interaction and bubble growth in the HBS structure. Here, we consider the bubble growth in completely recrystallized HBS. A representative microstructure with periodic boundary conditions is created with Voronoi tessellation with randomly specified existing bubbles. The simulation domain size is 1.25 μm $\times$ 1.25μm. The simulation domain is initialized with 100 grains of 100 nm size and a single bubble with varying radii of 100 nm, 150 nm, and 200 nm corresponding to approximately 2%, 4.5%, and 8% porosity, respectively. These porosity values are selected based on experimental porosity observed in regions adjacent to HBS locations [30]. We postulate that the microstructure in this region resembles the representative fuel microstructure prior to and at the initial recrystallization stage. The initial conditions created for this set of simulations are provided in Figure 4.

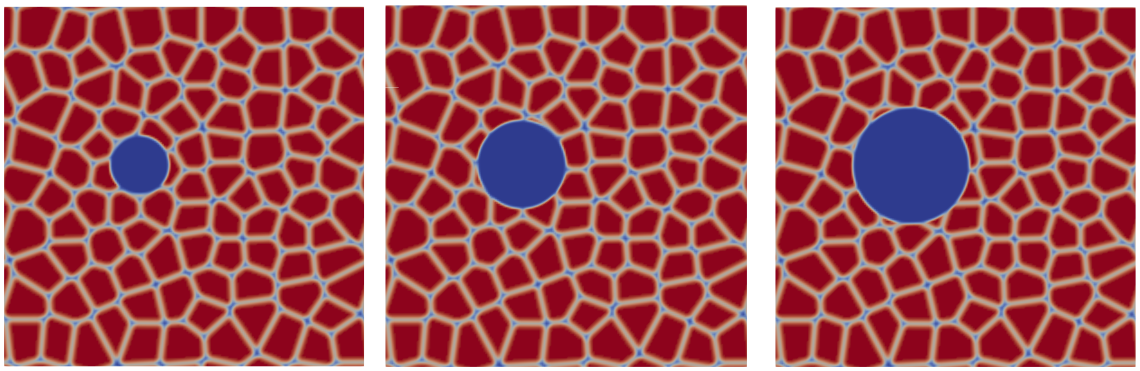

(a) (b) (c)

Figure 4: Sample initial HBS structure created with Voronoi tessellation with 100 nm (a), 150 nm (b) and 200 nm (c) bubble.

At the initial condition, the bubble is considered to maintain equilibrium pressure, determined by the Gibbs-Thomson condition, $P_{eq} = 2\gamma_{st}/r$, where γ_{st} is the surface tension and r is the bubble radius. Assuming $\gamma_{st} = \gamma$, equilibrium pressures for the bubble sizes considered are 30 MPa, 20 MPa, and 15 MPa. The initial gas concentration within the bubble is estimated from the van der Waals equation of state,

$$P_g = \frac{c_g k_B T}{\Omega - c_g b}. \tag{34}$$

Thus, at 1200 K, the initial gas concentration within the bubble is set at 0.0642, 0.0448, 0.0344 for the 100 nm, 150 nm, and 200 nm bubble, respectively. Corresponding vacancy concentration within the bubble is set, such that $c_v = 1 - c_g$. The matrix is initialized with a gas super saturation of 0.02 atomic fraction and vacancy concentration at the steady-state value. In addition, we consider enhanced gas and vacancy diffusion within bubbles and along interfaces. Since the physical diffusion values in the different interfacial regions are not known, we set $D_{v_b} = 1000 D_{v_m}$, $D_{v_s} = 100 D_{v_m}$, $D_{v_{GB}} = 100 D_{v_m}$ for vacancies and $D_{g_b} = 10^6 D_{g_m}$, $D_{g_s} = 10^5 D_{g_m}$, $D_{g_{GB}} = 10^5 D_{g_m}$ for gas atoms. Different enhancement factors are used so that both vacancies and gas atoms have diffusivities in the same order of magnitude except in the matrix. It was previously noted that these diffusion enhancement factors influence formation of new bubbles vs. growth of existing bubbles in the HBS regions [9]. The competition and combination of diffusion of different species is responsible for bubble growth and associated pressure increase in the HBS. Increase in vacancy concentration within bubbles leads to growth of the bubbles, whereas the increase in gas concentration increases the bubble pressure. With the current values, the model is able to capture growth of existing bubbles and formation of new intergranular and intra-granular bubbles concurrently while limiting numerical issues. Figure 5 shows the bubble evolution over time for the 100 nm bubble. At the initial stage, few intra-granular bubbles are formed within the grains. Gas atoms combined with the vacancies form these bubbles. Some these bubbles appear at nano-scales which is significant lower than our simulation scales and hence, these bubbles are not tractable in mesoscale simulations. Moreover, this causes significant numerical instabilities in the model. We have mitigated this issue by choosing appropriate diffusion enhancement factors. It is observed that these small bubbles are depleted over time, contributing to further growth of existing and newly formed intergranular bubbles. The bubble reaches 130.3 nm radius at the end of the simulation. At 5.71×10^3 sec, the gas pressure in the bubble reaches 175.36 MPa. However, as the bubble grows further, the bubble pressure is reduced and at the final stage the bubble pressure is 152.08 MPa.

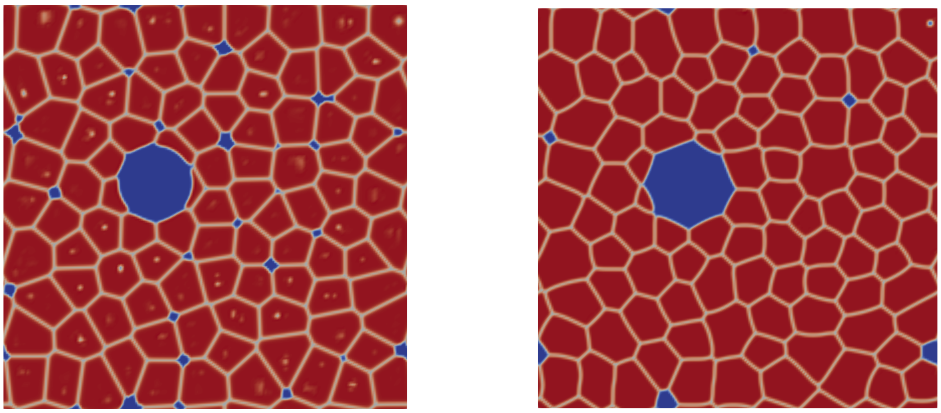

(a) (b)

Figure 5: Bubble evolution in HBS at time 5.71×10^3 sec (a) and 6.23×10^5 sec (b) for initial 100 nm bubble.

Figure 6 depicts the evolution of the 150 nm and 200 nm bubbles under the same conditions. The bubble pressures reached in these cases are 225.07 MPa and 123.79 MPa, respectively.

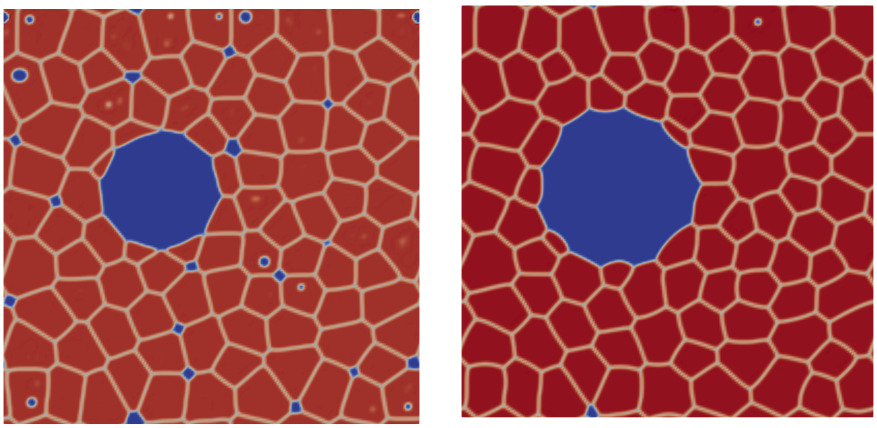

(a) (b)

Figure 6: Bubble evolution in HBS for initial 150 nm bubble at 6.58×10^4 sec (a) and initial 200 nm bubble at 4.87×10^5 sec (b).

Figure 7 captures the porosity evolution over time for different initial bubble sizes. When the porosity evolution is scaled with initial porosity (Figure 7b), the bubble growth rate decreases with increase in the initial bubble sizes. In all the cases, porosity increases significantly at the initial stage and stabilizes over time. At later stages, the bubbles coalesce and growth of existing bubbles occurs without altering the porosity. Furthermore, gas atoms accumulate within the bubbles resulting in overpressurization.

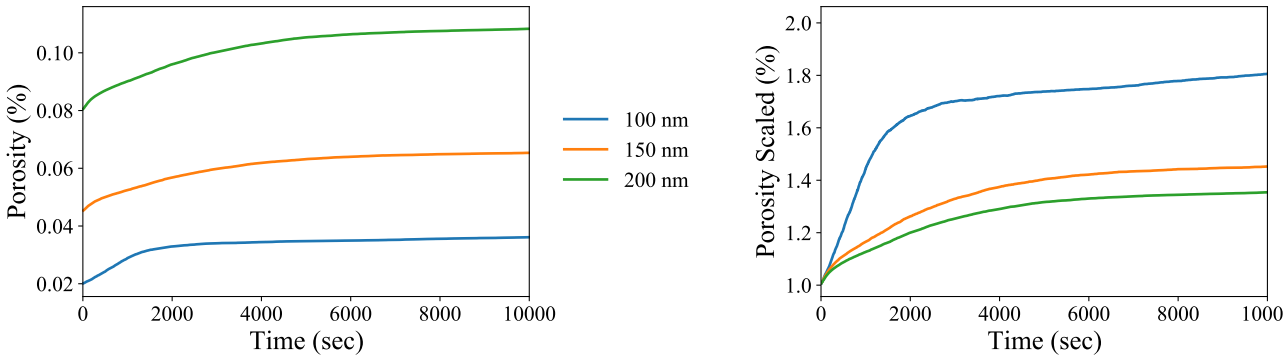

(a) (b)

Figure 7: Porosity evolution over time for different initial bubble sizes (a) and porosity comparison scaled with initial porosity (b).

Experimentally, the presence of an extremely high density of dislocations has been observed around the large bubbles in the HBS. It is hypothesized that these dislocations are created when bubble pressure exceeds the dislocation punching pressure for UO_2 as the HBS forms. Hence, the bubble pressures are expected to be at or above dislocation punching pressure [6]. The analytical pressure value determined by the dislocation punching criterion is calculated as

$$P = P_{eq} + P_{ext} = P_h + \frac{2\gamma_{st}}{r} + \frac{Gb}{r}, \tag{35}$$

where P_{eq} is the equilibrium pressure, and P_{ext} is the external pressure, P_h is the hydrostatic pressure, γ_{st} is the surface tension, r is the bubble radius, G is the shear modulus, and b is the burger's vector.

Figure 8 compares the bubble pressure calculated from the simulations to the analytical values obtained from Equation 35 assuming the hydrostatic pressure to be zero. The pressure values obtained from the simulations are close to or above the analytical dislocation punching pressure. However, for the 150 nm bubble, the simulation pressure value is significantly higher than what the analytical dislocation punching criteria indicate. This indicates that dislocation punching may contribute significantly to HBS bubble growth, which is not accounted for in the present model.

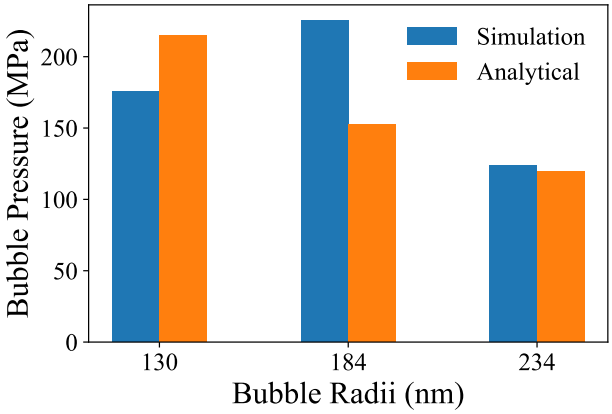

Figure 8: Bubble pressure calculated from the simulations compared against the dislocation punching criteria.

Figure 9 compares the growth of a 150 nm bubble at 1200 K and 1100 K. The bubble growth rate reduces with decrease in temperature. Reduction in diffusivity with temperature hinders the bubble growth at lower temperature. However, higher Xe concentration is achieved within the bubble at 1100 K temperature. The bubble reaches a maximum pressure of 424.78 MPa in this case. Further verification and validation of the pressure calculated from the model is necessary.

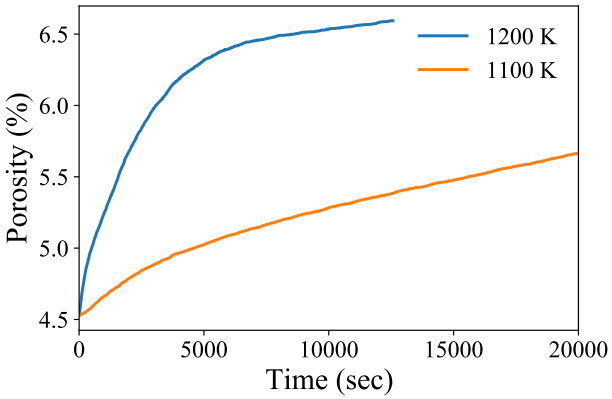

Figure 9: Porosity evolution over time for 150 nm bubble at 1200 K and 1100 K temperature.

2.3 Conclusion

A grand-potential based phase field model has been developed to concurrently capture the bubble growth and pressure increase in the HBS. The competition between vacancies and gas atoms drives the bubble growth vs. pressure increase in the bubble. The pressure predicted by the model compares reasonably well with

the dislocation punching criteria. Further verification and validation of the pressure values is required. The pressure values calculated from these simulations can be used to inform the fragmentation criteria at the engineering scale. Moreover, the structures generated from this model can be used for mesoscale fracture simulation and also can provide crucial information pertaining to HBS structures to engineering scale models for performance evaluation.

The model, at its present state, certainly has some limitations. The model currently only tracks vacancies and gas atoms. Consideration of other defects such as interstitials is required to make the model more predictive. Incorporation of the cluster-dynamics data needs to be done for better connectivity between calculations at different scales. Moreover, 3D analysis could potentially provide more insight into the bubble evolution and pressure. Finally, more quantitative verification and validation of the model needs to be done to accurately inform the engineering scale performance models.

3 PHASE-FIELD SIMULATIONS OF FISSION GAS BUBBLES IN HIGH BURNUP UO_2 DURING STEADY-STATE AND LOCA TRANSIENT CONDITIONS

3.1 Introduction

To inform the development of a mechanistic criterion for pulverization, this section seeks to address two primary questions using phase-field modeling. The first question is whether bubble sizes change during a typical LOCA transient. Bubble sizes could be expected to change during a LOCA by the following mechanism. Due to the rapid rise in temperature, the pressure of the gas contained within the bubble also increases rapidly. This increase in gas pressure causes the bubble to become even more overpressurized relative to equilibrium than at the start of the transient; thus, a greater compressive stress is experienced in the fuel matrix surrounding the bubble. This compressive stress leads to a greater driving force for vacancy flux, potentially leading to rapid growth of the bubble (if pulverization does not occur first). However, it is unknown whether such growth will be significant during the short duration of a LOCA transient. The second question we address is that of determining what pressure transients are experienced in the bubble in response to a LOCA. In future work, these pressure transients can be used as input to a fracture model to determine whether pulverization occurs for a given transient.

To address these questions, a new phase-field model is developed based on the Kim-Kim-Suzuki (KKS) formulation [31]. Several phase-field models have been developed to simulate the fission gas bubble microstructure for UO_2 fuel in the literature [32, 33, 34, 35, 36, 14, 37]. Given the expected overpressurization of bubbles during a LOCA transient, the balance between gas pressure and the surface tension of the matrix-bubble interface is an important physical effect that should be included in the model for the present study. To our knowledge, Reference [37] is the only phase-field model thus far that includes the bubble-size-dependent surface tension in the mechanical equilibrium condition and thus its effects on the stress state of the surrounding fuel. Here, we implement an alternative approach, based on Reference [38], that allows the curvature of an arbitrarily-shaped interface to determine surface tension forces. The model is implemented in INL's Marmot application for phase-field simulation of nuclear materials.

The structure of this section is as follows. In Section 3.2, the formulation of the model is given, including the surface tension effects and parameterization of the model for conditions typical of the region where the HBS has formed. In Section 3.3, the implementation of the gas pressure and surface tension is verified for equilibrium, underpressurized, and overpressurized bubbles. The model is applied to steady-state and transient conditions in Section 3.4. The growth of single bubbles and the impingement of multiple bubbles during steady-state growth are simulated in Sections 3.4.1 and 3.4.2, respectively. The response of bubbles in the HBS region to transient conditions is considered in Section 3.4.3. The initial bubble pressure, size, average porosity, and external restraint pressures are varied parametrically under typical LOCA conditions, and the resulting pressure transients are calculated. Finally, in Section 3.5, conclusions are drawn, and an outlook for future work is given.

3.2 Model Formulation

The model for UO_2 gas bubble swelling is formulated following that proposed by Kim et al. [31], typically referred to as the "KKS" formulation. The model is extended from that in Reference [31] to include two tracked species: namely, the normalized concentration (site fraction) of uranium site vacancies, c_v, and the normalized concentration of gas atoms, c_g (assumed to be represented by the properties of Xe atoms), which sit on U site positions in the UO_2 lattice. Because the concentration of U interstitials is significantly lower than the vacancy concentration during steady-state reactor operation [39], interstitials are not considered

here. In addition to the concentrations of vacancies and gas atoms, the model also indicates the difference between matrix (solid) and bubble phases with a non-conserved order parameter, η, that varies continuously from 0 in the matrix phase to 1 in the bubble phase. As in [14], the bubble phase is considered to be a mixture of U-site vacancies and gas atoms such that $c_v + c_g = 1$.

The total free energy F of the system is given by

$$F = \int_V \left[f_{chem} + W g(\eta) + \frac{\kappa}{2} |\nabla \eta|^2 + f_{el} \right] \, \mathrm{d}V, \tag{36}$$

where f_{chem} is the chemical contribution to the free energy density, $g(\eta) = \eta^2(1-\eta)^2$ is a double-well potential, W is the height of the double well, κ is the gradient energy coefficient, and f_{el} is the elastic energy density.

3.2.1 Chemical free energy density

The chemical free energy density is formulated in terms of the free energy densities of the possible phases within the system:

$$f_{chem} = [1 - h(\eta)] f^m_{chem}(c^m_v, c^m_g) + h(\eta) f^b_{chem}(c^b_v, c^b_g) \tag{37}$$

where f^b_{chem} is the chemical free energy density of the bubble phase; f^m_{chem} is the chemical free energy density of the matrix phase; c^b_v and c^b_g are the concentrations of vacancies and gas, respectively, in the bubble phase; and c^m_v and c^m_g are the concentrations of vacancies and gas, respectively, in the matrix phase. The function $h(\eta) = \eta^3(6\eta^2 - 15\eta + 10)$ is an interpolation function that varies smoothly from $h(0) = 0$ to $h(1) = 1$.

Assuming that the matrix phase can be treated as an ideal solution, its free energy density can be expressed as

$$f^m_{ideal} = \frac{kT}{V_a} \left[c^m_v \ln c^m_v + c^m_g \ln c^m_g + (1 - c^m_g - c^m_v) \ln(1 - c^m_g - c^m_v) \right] + \frac{c^m_v G^v_f}{V_a} + \frac{c^m_g G^g_f}{V_a} \tag{38}$$

where k is Boltzmann's constant, T is the temperature in K, V_a is the atomic volume occupied by a single U atom, and G^j_f is the Gibbs free energy of formation of defect species j. $G^j_f = H^j_f - TS^j_f$, where H^j_f is the enthalpy of formation of defect j and S^j_f is its entropy of formation. Numerical values for these and other model parameters are given in Table 2. The values for H^v_f and S^v_f were taken from the literature. The value for H^g_f was calculated as the solution energy (sum of trap site formation energy and incorporation energy [40]) for Xe in a bound uranium-oxygen vacancy cluster, which was found to be the most stable trap site for Xe [20]. The value for S^g_f was calculated in the same manner.

To improve the numerical performance of the model, a parabolic approximation to f^m_{ideal} will be used:

$$f^m_{ideal} \approx f^m_{chem} = \frac{k^m_v}{2}(c^m_v - c^{m,min}_v)^2 + \frac{k^m_g}{2}(c^m_g - c^{m,min}_g)^2 \tag{39}$$

The parabolic approximation for the vacancy contribution to f^m_{chem} is parameterized such that vacancies will have the same chemical potential in the parabolic approximation as they do in the ideal solution model at the steady-state defect concentration that exists during reactor operation, c^0_v. This is to ensure that the same driving force for defect flux exists in the parabolic approximation as in the ideal solution model [35], since defect fluxes are driven by gradients in chemical potential. For vacancies, this condition can be expressed as

$$\mu_v = \left. \frac{\partial f^m_{ideal}}{\partial c^m_v} \right|_{c^0_v} = \left. \frac{\partial f^m_{chem}}{\partial c^m_v} \right|_{c^0_v} \tag{40}$$

The minimum in the parabola is set to the equilibrium concentration of vacancies in the absence of irradiation: $c_v^{m,min} = \exp\left(\frac{-G_f^v}{kT}\right)$. The parabola curvature is determined by substituting Equations (38) and (39) into Equation (40) and re-arranging

$$k_v^m \approx \frac{1}{\left(c_v^0 - c_v^{m,min}\right)}\left[\frac{kT}{V_a}\ln c_v^0 + \frac{G_v^f}{V_a}\right] \tag{41}$$

(where the $\ln(1 - c_v^m - c_g^m)$ term has been neglected since it is much smaller than $\ln c_v^0$ for dilute defect species concentrations). For temperatures less than 1300 K, $c_v^0 \approx 8 \times 10^{-3}$ [39]. Equation (41) was solved for values in the range of 700 K $\leq T \leq$ 1300 K, and the parabola curvature was fit to a linear function of T, resulting in $k_v^m = 3.17 \times 10^{10}$ J/m^3 + $1.79 \times 10^8 T$ J/m^3/K. For gas atoms, the minimum in the parabola was set to $c_g^{m,min} = \exp\left(\frac{-G_f^g}{kT}\right)$ as for vacancies. Unlike vacancy concentration, the gas atom concentration is not held at a local steady-state value by a recombination term. Therefore, for simplicity, $k_g^m = k_v^m$ was chosen as in Reference [14].

The bubble phase is considered to be a mixture of gas atoms and U-site vacancies. The chemical free energy of the bubble phase is given by

$$f_{chem}^b = c_g^b \frac{kT}{V_a}\left[\ln\left(\frac{1}{n_Q(\frac{V_a}{c_g^b} - b)}\right) - 1\right] + \frac{k_p}{2}(1 - c_v^b - c_g^b)^2 + f_0 \tag{42}$$

The first term represents the free energy density of a van der Waals gas [17]. $n_Q = \left(\frac{mkT}{2\pi\hbar}\right)^{3/2}$ is the quantum concentration, m is the mass of a Xe atom, and $b = 0.085$ nm^3/atom is the hard-sphere exclusion volume of Xe in the van der Waals equation of state [16]. The second term is a penalty term that prevents solid U atoms from entering the gas phase by introducing a penalty for compositions where $c_g^b + c_v^m = 1$ does not hold. Conceptually, it can be thought of as a constraint that maintains the gas phase composition along the xenon-vacancy edge of the Gibbs triangle representing the system's composition [14]. The value of the prefactor $k_p = 6.4 \times 10^{11}$ J/m^3 was chosen to maintain $c_g^b + c_v^m$ within 0.2% of 1.0. The third term controls the offset between the gas phase and solid phase free energies, f_0. This offset was used to set the minima of the free energy densities of the matrix and bubble phases to have the same minimum value, as in [14]. A temperature-dependent value of f_0 was fit, resulting in $f_0 = 2.25 \times 10^8$ J/m^3 - $2.04 \times 10^6 T$ J/m^3/K.

3.2.2 Elastic energy density

The model uses the Voigt-Taylor scheme to interpolate the elastic energy densities, stresses, and strains [41, 42] since it allows the gas bubble pressure to be incorporated in the mechanical equilibrium equation in a straightforward manner. The elastic energy density f_{el} is formulated as

$$f_{el} = [1 - h(\eta)]f_{el}^m + h(\eta)f_{el}^b \tag{43}$$

where f_{el}^m is the elastic energy density of the matrix phase, and f_{el}^b is the elastic energy density of the bubble phase. (A small elastic energy density is defined in the bubble phase solely to prevent discontinuities in the displacement field at the interfaces and is parameterized such that its contribution to microstructural evolution is negligible, as discussed further in this section.) The elastic energy density in the matrix phase is given by

$$f_{el}^m = \frac{1}{2}C_{ijkl}^m \epsilon_{ij}^{el,m} \epsilon_{kl}^{el,m} \tag{44}$$

and in the bubble phase, by

$$f_{el}^{b} = \frac{1}{2} C_{ijkl}^{b} \epsilon_{ij}^{el,b} \epsilon_{kl}^{el,b} \tag{45}$$

The stress tensor is also interpolated using the order parameter. Using the Voigt-Taylor scheme, the mechanical equilibrium equation has the form

$$\nabla \cdot \sigma_{ij} = \nabla \cdot \left[[1 - h(\eta)] \sigma_{ij}^{m} + h(\eta) \sigma_{ij}^{b} + \sigma_{ij}^{st} \right] = 0 \tag{46}$$

where σ_{ij}^{m} is the stress tensor in the matrix phase, σ_{ij}^{b} is the stress tensor in the bubble phase, and σ_{ij}^{st} is the surface tension of the matrix-bubble interface. The stress tensor in the matrix phase σ_{ij}^{m} is given by

$$\sigma_{ij}^{m} = C_{ijkl}^{m} \epsilon_{kl}^{el,m} \tag{47}$$

where C_{ijkl}^{m} is the matrix phase stiffness tensor and $\epsilon_{ij}^{el,m}$ is the local elastic strain. The stiffness tensor components C_{ijkl}^{m} are taken from Reference [27] and are listed in Table 2. The local elastic strain is given by

$$\epsilon_{ij}^{el,m} = \epsilon_{ij} - \epsilon_{ij}^{*} = \epsilon_{ij} - (c_{v}^{m} - c_{v}^{0}) \epsilon_{v}^{0} \delta_{ij} \tag{48}$$

where ϵ_{ij} is the total strain and ϵ_{ij}^{*} is the eigenstrain in the matrix due to defects. The concentration of gas atoms during reactor operation is expected to be small (on the order of 10^{-7} [20]) compared to steady-state vacancy concentration. Thus, the eigenstrain due to gas atoms is neglected, and only the eigenstrain due to vacancies is considered. This results in $\epsilon_{ij}^{*} = (c_{v}^{m} - c_{v}^{0}) \epsilon_{v}^{0} \delta_{ij}$, where ϵ_{v}^{0} is a constant factor that describes the local contraction of the lattice due to the difference between the local vacancy concentration and the steady-state vacancy concentration in the bulk far from bubbles, and δ_{ij} is the Dirac delta function. The value of ϵ_{v}^{0} was determined to be -0.269 from density functional theory calculations, assuming isotropic contraction, following the methodology in Reference [43]. (For these calculations, vacancies are assumed to be neutralized by the presence of U^{5+} ions, which best captures the physical state of the material [44, 45].)

The stress tensor in the bubble phase σ_{ij}^{b} is controlled by the density of gas in the bubble using the van der Waals equation of state, with a small elastic contribution added to ensure that the displacement fields remain continuous in the interfacial region. The resulting expression is

$$\sigma_{ij}^{b} = -\left(\frac{kT}{\frac{V_a}{c_g^b} - b} \right) \mathbf{I} + C_{ijkl}^{b} \epsilon_{kl}^{el,b} \tag{49}$$

where $\mathbf{I}$ is the second-order identity tensor, $C_{ijkl}^{b} = 10^{-3} C_{ijkl}^{m}$ to ensure that the elastic energy contribution from the bubble phase has a negligible contribution to the system's evolution, and $\epsilon_{ij}^{el,b} = \epsilon_{ij}$. The negative sign in the first term is to ensure that the gas exerts a compressive stress on the matrix at the bubble-matrix interface.

The surface tension of the matrix-bubble interface is based on the approach developed in Reference [38] and is given by

$$\sigma_{ij}^{st} = \left[W g(\eta) + \frac{\kappa}{2} |\nabla \eta|^2 \right] \mathbf{I} - \kappa \nabla \eta \otimes \nabla \eta \tag{50}$$

where $\otimes$ denotes the dyadic product. This term is non-zero only in the interfacial region, and the surface tension and interfacial energy are assumed to be the same in this approach, resulting in the use of the same W and κ as used in Equation (36). If future experimental or computational data reveal that surface tension and interfacial energy differ significantly, different values of W and κ would be required in Equations (36) and (50).

3.2.3 KKS system constraints

The overall concentrations are defined in terms of the phase concentrations as [31]

$$c_v = [1 - h(\eta)]c_v^m + h(\eta)c_v^b \tag{51}$$

and

$$c_g = [1 - h(\eta)]c_g^m + h(\eta)c_g^b \tag{52}$$

In addition, the KKS model requires that the local chemical potentials of a component be equal to each other in each phase [31]:

$$\mu_g = \frac{df_T^b}{dc_g^b} = \frac{df_T^m}{dc_g^m} \tag{53}$$

and

$$\mu_v = \frac{df_T^b}{dc_v^b} = \frac{df_T^m}{dc_v^m} \tag{54}$$

where $f_T^m = f_{chem}^m + f_{el}^m$ and $f_T^b = f_{chem}^b + f_{el}^b$.

3.2.4 Interfacial energy parameterization

We estimate the interfacial energy γ between the matrix and bubble as follows. In Reference [46], grain boundary energies in UO_2 were estimated to lie in a range centered at approximately 1.5 J/m^2. Using a representative grain boundary bubble semi-dihedral angle of 50°, γ can be estimated using Young's equation to be 1.17 J/m^2.

In the KKS model, the interfacial energy and interface thickness 2λ are related to the gradient energy coefficient and double-well potential height via the following analytical expressions:

$$\gamma = \frac{\sqrt{\kappa W}}{3\sqrt{2}} \tag{55}$$

$$2\lambda = 2.2\sqrt{2}\sqrt{\frac{\kappa}{W}} \tag{56}$$

where the interface thickness 2λ is defined as the distance between $\eta = 0.1$ and $\eta = 0.9$. For the majority of the simulations, 2λ was chosen to be 100 nm, such that it is an order of magnitude smaller than the bubble sizes. With γ and 2λ specified, Equations (55) and (56) can be rearranged to determine the required values of κ and W to be $\kappa = 1.60 \times 10^{-7}$ J/m and $W = 1.54 \times 10^8$ J/m^3.

3.2.5 Evolution equations

The order parameters evolve by the Allen-Cahn equation as

$$\frac{\partial \eta}{\partial t} = -L\left(\frac{\delta F}{\delta \eta}\right) \tag{57}$$

where L is the order parameter mobility for η. Using Equations (27) and (28) of Reference [31], this can be written as

$$\begin{aligned}\frac{\partial \eta}{\partial t} &= L\left[\frac{dh}{d\eta}\left[(f_T^m - f_T^b) - \mu_v(c_v^m - c_v^b) - \mu_g(c_g^m - c_g^b)\right] - W\frac{dg}{d\eta} + \kappa\nabla^2\eta\right] \\ &= L\left[\frac{dh}{d\eta}\left[(f_{chem}^m + f_{el}^m - f_{chem}^b - f_{el}^b) - \mu_v(c_v^m - c_v^b) - \mu_g(c_g^m - c_g^b)\right] - W\frac{dg}{d\eta} + \kappa\nabla^2\eta\right]\end{aligned} \tag{58}$$

The concentration of each defect species evolves as

$$\frac{\partial c_v}{\partial t} = \nabla \cdot M_v \nabla \mu_v + s_v - K_v c_v^m \tag{59}$$

$$\frac{\partial c_g}{\partial t} = \nabla \cdot M_g \nabla \mu_g + s_g \tag{60}$$

where M_g and M_v are the mobilities of the defect species, s_v and s_g are source terms accounting for the production of each defect, and K_v is an effective sink term for vacancies that accounts for the effects of interstitial-vacancy recombination and vacancy absorption at sinks. The source terms are of the form $s_v = s_v^0[1-h(\eta)]$ and $s_g = s_g^0[1-h(\eta)]$, where s_v^0 and s_g^0 are the constant values of defect production in the matrix phase, and the function $[1-h(\eta)]$ limits defect production to the matrix phase only. The Xe production rate $s_g^0 = \dot{F} Y_{Xe} V_a$ is determined from the fission rate density, $\dot{F}$, and the fission yield of Xe, Y_{Xe}. The constant V_a converts from number density to a normalized concentration. We have assumed $F = 1.09 \times 10^{13}$ fissions/cm^3/s, based on typical values for LWR operation [16] and $Y_{Xe} = 0.2156$ [47]. s_v^0 is assumed to be $10^4 \dot{F} V_a$ [39].

Since the phase-field model employed in this work does not track interstitials, the purpose of the effective sink term $-K_v c_v^m$ is to maintain the vacancy concentration in the matrix at steady-state conditions far from any large HBS bubbles at $c_v^0 \approx 8 \times 10^{-3}$, as was determined from cluster dynamics simulations for the temperatures of interest in this work [39]. At steady-state far from any large HBS bubbles or sinks, the vacancy concentration is constant both time and position, so $\frac{\partial c_v}{\partial t} = 0$ and $\nabla \mu_v = 0$. Under these conditions, from Equation (59),

$$K_v = \frac{s_v^0}{c_v^0} = 5.12 \times 10^{-4} \text{ s}^{-1} \tag{61}$$

The defect mobilities were calculated from the diffusion coefficients and second derivatives of free energies for each phase as in Equation (18) of Reference [31]:

$$M_g = \frac{D_g(\phi)}{f_{c_g c_g}} = \frac{h D_g^b + (1-h) D_g^m}{f_{c_g c_g}} \tag{62}$$

where $f_{c_g c_g}$ is as defined in Equation (29) of Reference [31]:

$$f_{c_g c_g} = \frac{\frac{d^2 f_T^m}{dc_g^2} \frac{d^2 f_T^b}{dc_g^2}}{[1-h(\eta)] \frac{d^2 f_T^b}{dc_g^2} + h(\eta) \frac{d^2 f_T^m}{dc_g^2}} \tag{63}$$

Within the matrix phase, Equation (63) reduces to $f_{c_g c_g} = \frac{d^2 f_T^m}{dc_g^2}$.

For the relatively low temperatures considered in the present simulations, the Xe diffusivity in the matrix phase is given by the athermal diffusivity $D_g^m = D_3 = 8.5 \times 10^{-40} \dot{F} = 9.3 \times 10^{-3}$ nm^2/s [20, 19]. Within the matrix phase, $d^2 f / dc_g^2 = k_v^m$. Since the diffusivity of Xe in the bubble phase is expected to be significantly higher than in the matrix, we set $D_g^b = 10^4 D_g^m$ and assume $f_{c_g c_g} = d^2 f_T^m / dc_g^2 = k_g^m$ throughout the simulation domain, which ensures that gas diffusivity and corresponding mobility is always significantly greater in the bubble phase than in the matrix phase. Testing with higher diffusion coefficients in the bubble phase did not cause any significant changes in the results.

Similarly, the vacancy mobility was calculated using

$$M_v = \frac{h D_v^b + (1-h) D_v^m}{f_{c_v c_v}} \tag{64}$$

Parameter	Value	Source
V_a	0.04092 nm^3	[26]
H_f^v	0.066 eV	[39]
S_f^v	$-9.0k$	[39]
H_f^g	3.50 eV	Section 3.2.1
S_f^g	$-80.61k$	Section 3.2.1
$c_v^{m,min}$	$\exp\left(\frac{-G_f^v}{kT}\right)$	Section 3.2.1
k_v^m	3.17×10^{10} J/m^3 + $1.79\times10^8 T$ J/m^3/K	Section 3.2.1
$c_g^{m,min}$	$\exp\left(\frac{-G_f^g}{kT}\right)$	Section 3.2.1
k_g^m	3.17×10^{10} J/m^3 + $1.79\times10^8 T$ J/m^3/K	Section 3.2.1
b	0.085 nm^3/atom	[16]
k_p	6.4×10^{11} J/m^3	Section 3.2.1
f_0	2.25×10^8 J/m^3 - $2.04\times10^6 T$ J/m^3/K	Section 3.2.1
C^m_{1111}	395 GPa	[27]
C^m_{1122}	121 GPa	[27]
C^m_{1212}	64 GPa	[27]
C^b_{ijkl}	$10^{-3}C^m_{ijkl}$	Section 3.2.2
ϵ_v^0	-0.269	Section 3.2.2
κ	1.60×10^{-7} J/m	Section 3.2.4
W	1.54×10^8 J/m^3	Section 3.2.4
s_g^0	9.62×10^{-11} s^{-1}	Section 3.2.5
s_g^0	4.09×10^{-6} s^{-1}	Section 3.2.5
K_v	5.12×10^{-4} s^{-1}	Section 3.2.5
D_g^m	9.3×10^{-3} nm^2/s	[19]
D_v^m	0.96 nm^2/s	Section 3.2.5
L	1.56×10^{-10} m^3/J/s	Section 3.2.5

Table 2: Parameters used for phase-field simulations of HBS bubble growth and pressure transients.

The vacancy diffusion coefficient in the matrix, D_v^m, is estimated from the experimentally measured self-diffusion coefficient D_U using $D_v^m = D_U/(\alpha_V c_v^0)$ [39], where $\alpha_V = 0.781$ is the correlation factor for vacancies [48]. For $T < 1400$ K under irradiation, uranium self-diffusion is in the athermal regime and $D_U = 6.0\times10^{-3}$ nm^2/s [22], resulting in $D_v^m = 0.96$ nm^2/s. D_v^b was set to $10^3 D_v^m$ and $f_{c_v c_v} = d^2 f_T^m/dc_v^2 = k_v^m + 3(C^m_{1111}+C^m_{1122})(\epsilon_v^0)^2$ was used throughout the simulation domain to ensure vacancy mobility was always significantly greater in the bubble phase than in the matrix phase.

The Allen-Cahn mobility L was set sufficiently high that interface motion was controlled by diffusion of defect species, resulting in $L = 1.56\times10^{-10}$ m^3/J/s. It was verified that changes in L above this value did not affect the bubble growth rate.

The evolution equations (58), (59), (60), (51),(52), (53),(54), and (46) were non-dimensionalized using the characteristic energy scale $E^* = C^m_{1212} = 64\times10^9$ J/m^3, length scale $l^* = 1$ nm, and time scale $\tau^* = 1$ s, and discretized using the finite element method as implemented in the MOOSE framework [49]. For simulations with spherical symmetry, the problem is solved in spherical coordinates, with symmetry allowing the problem to be solved in 1D as a function of the radial coordinate r only. In this case, 1D elements are

used with linear Lagrange shape functions. Mesh size is discussed in Section 3.3. For 3D simulations, a Cartesian coordinate system is used with 3D hexahedral mesh elements (with $\Delta x = \Delta y = \Delta z$) and linear Lagrange shape functions.

Natural boundary conditions are used, resulting in no-flux boundary conditions for chemical species, a zero-gradient condition for η, and traction-free boundary conditions for the mechanical equilibrium equation. Time integration uses the second-order backward differentiation formula. The evolution equations are solved at each time step using the preconditioned Jacobian-Free Newton-Krylov method. Adaptive time stepping is used using the IterationAdaptiveDT algorithm as implemented in the MOOSE framework [50].

3.3 Model Verification

3.3.1 Equilibrium bubbles

Prior to investigating LOCA transients, the behavior of the model described in Section 3.2 is verified to ensure that it correctly captures the balance between gas pressure and surface tension. A bubble with the equilibrium pressure $P = 2\gamma_{st}/R$, where γ_{st} is the surface tension and R is the radius of the bubble [16], is first considered. An analytical solution exists for the stress state of a solid surrounding a pressurized gas bubble in the sharp interface limit [51]. When the radius of the surrounding solid is much larger than the radius of the bubble and there is no external pressure on the external surface of the solid, the stress tensor component σ_{rr} in spherical coordinates is given by

$$\sigma_{rr} = -\frac{R^3}{r^3}\left(P - \frac{2\gamma_{st}}{R}\right) \tag{65}$$

for $r > R$. In this work, we assume that the surface tension is equal to the interfacial energy, $\gamma_{st} = \gamma$. As can be seen from Equation 65, for an equilibrium bubble with $P = 2\gamma_{st}/R$, $\sigma_{rr} = 0$ in the surrounding solid.

To verify that the model correctly captures this behavior, a bubble with $R = 250$ nm was simulated. The equilibrium pressure for a bubble with this radius is 9.36 MPa, and the corresponding $c_g = 0.03662$ and $c_v = 1 - c_g = 0.96338$. The simulation domain used spherical coordinates with spherical symmetry assumed, and had a radius of 550 nm so that the gas phase porosity was 10%. The initial condition for the order parameter was

$$\eta = \frac{1}{2}\left[1 + \tanh\left(\frac{r - R}{\sqrt{2}\delta_\eta}\right)\right] \tag{66}$$

where $R = 250$ nm and δ_η is the equilibrium thickness of the interfacial profile [31]. The initial conditions for the gas and vacancy concentrations were

$$c_g = c_g^{b,i} h(\eta) + c_g^{m,i}(1 - h(\eta)) \tag{67}$$

$$c_v = c_v^{b,i} h(\eta) + c_v^{m,i}(1 - h(\eta)) \tag{68}$$

where $c_g^{b,i} = 0.03662$, $c_v^{b,i} = 0.96338$, $c_g^{m,i} = 10^{-7}$, and $c_v^{m,i} = 0.008$, and η is given by Equation 66. For the purposes of verification of the balance between surface tension and gas pressure, the eigenstrain prefactor ϵ_v^0 was set to 0 to prevent non-equilibrium vacancy concentrations in the interface from affecting the stress calculation. All other simulation parameters were as shown in Table 2, with the exception that κ and W were changed to vary the interface width 2λ from 16.67 to 100 nm in order to investigate the effect of interface width on the stress state. The grid spacing $\Delta x = 2\lambda/10$. The simulation was allowed to run for a single time step of 0.5 s.

The σ_{rr} component of the stress tensor is shown in Figure 10a for varying 2λ, along with the analytical solution from Equation (65). The gas pressure inside the bubble results in $\sigma_{rr} = -P = -9.36$ MPa inside the

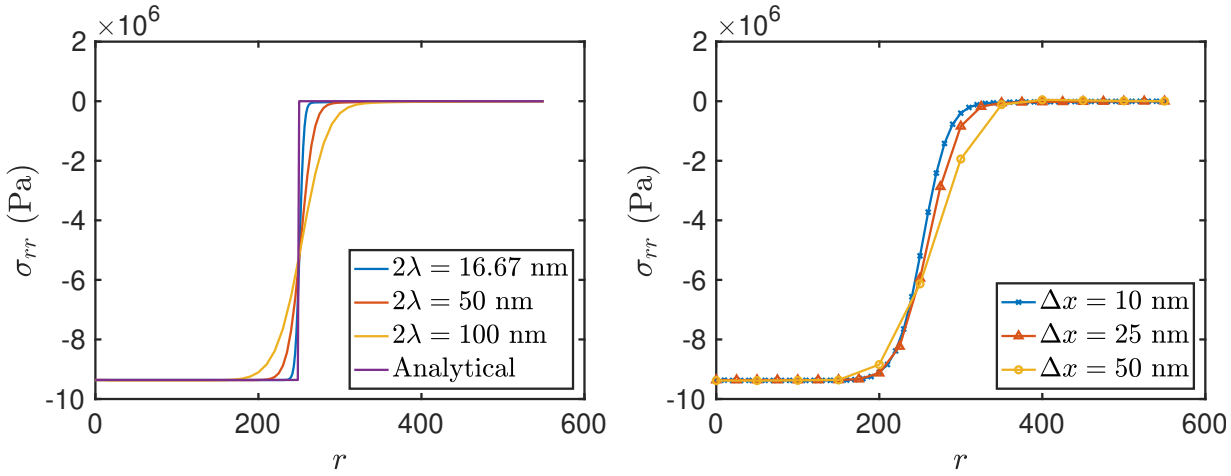

Figure 10: (a) σ_{rr} as a function of radius for a gas bubble with $R = 250$ nm and the expected equilibrium pressure of $P = 9.36$ MPa for varying interface width 2λ, together with the analytical solution. Because the surface tension of the bubble-matrix interface exactly balances the gas bubble pressure, $\sigma_{rr} = 0$ outside the bubble. (b) Effect of grid spacing Δx on stress state outside the bubble for $2\lambda = 100$ nm.

bubble ($r < R - \lambda$). In each case, $\sigma_{rr} = 0$ outside the bubble ($r > R + \lambda$). This demonstrates that the model correctly reproduces the expected behavior: because the surface tension exactly balances the gas pressure, no compressive or tensile stress in the radial direction is present in the fuel matrix surrounding the bubble. Even for $2\lambda = 100$ nm, the stress state outside the bubble is correctly captured.

The effect of grid spacing Δx was also considered, as shown in Figure 10b for $2\lambda = 100$ nm. Slight deviations in the stress profile were observed as Δx was increased from 10 to 50 nm. Based on the relatively close agreement in the stress profiles between $\Delta x = 10$ and 25 nm, $\Delta x = 2\lambda/4$ was used at the finest level of mesh refinement for the simulations of Section 3.4 in order to improve computational efficiency. In all cases, $\sigma_{rr} = 0$ was obtained sufficiently far from the interface, as expected.

3.3.2 Non-equilibrium bubbles

The behavior of the model for bubbles with gas pressures different from equilibrium is considered in this section. As can be seen from the analytical solution of Equation (65), for an overpressurized bubble, or a bubble with gas pressure higher than the equilibrium pressure for its radius, a compressive stress will be exerted on the surrounding fuel matrix in the radial direction ($\sigma_{rr} < 0$). Conversely, for an underpressurized bubble, a tensile stress will be felt in the surrounding fuel matrix in the radial direction ($\sigma_{rr} > 0$). The analytical solution of Equation 65 gives σ_{rr} as a function of radius.

To test whether the model can correctly reflect this behavior, a bubble with $R = 250$ nm is again considered, with an expected equilibrium pressure of 9.36 MPa. To test the behavior for an overpressurized condition, a bubble with $P = 15$ MPa is considered. Simulation parameters and initial conditions were as described in Section 3.3.1, except that $c_g^{b,i} = 0.05611$ and $c_v^{b,i} = 0.94389$, and the simulation domain had a radius of 1000 nm so that the analytical solution better matched the zero-traction boundary condition employed in the simulation. The σ_{rr} component of the stress tensor at the end of the simulation is shown in Figure 11a as a function of the interface width 2λ. Outside the bubble, $\sigma_{rr} < 0$, indicating that a compressive stress is exerted on the matrix in the radial direction, as expected for an overpressurized bubble. As the interface width was decreased, the simulation results converged to the analytical solution, as expected. For all

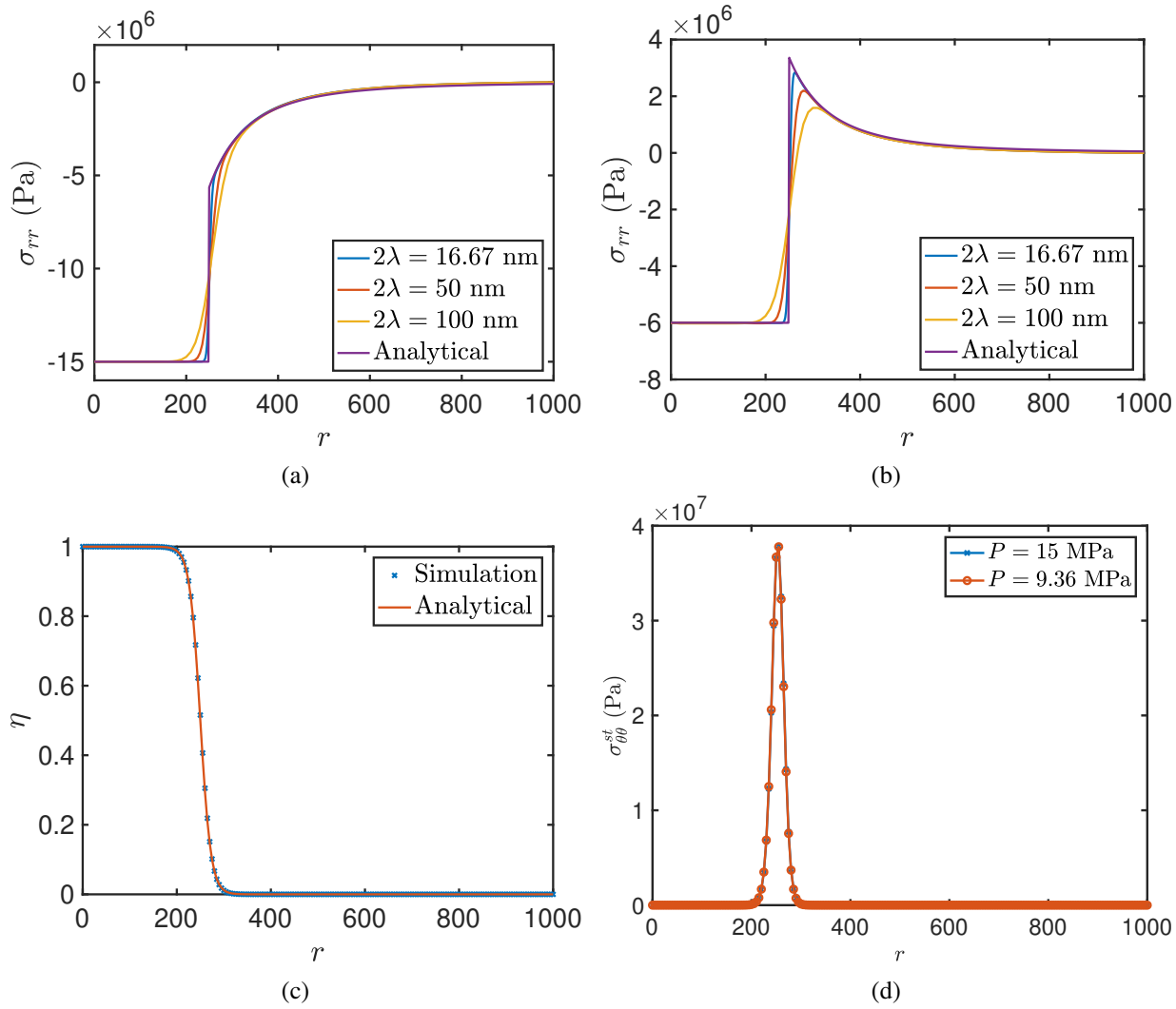

Figure 11: (a) Stress tensor component σ_{rr} for an overpressurized bubble for varying interface width 2λ and comparison to analytical solution. In the fuel matrix outside the bubble, $\sigma_{rr} < 0$, corresponding to a compressive stress in the radial direction. (b) Stress tensor component σ_{rr} for an underpressurized bubble. In the fuel matrix outside the bubble, $\sigma_{rr} > 0$, corresponding to a tensile stress in the radial direction. (c) Order parameter profile η for an overpressurized bubble with $P = 15$ MPa at $t = 10^6$ s and comparison to analytical solution for $2\lambda = 50$ nm. The elastic energy in the interface does not cause significant deviation of η from the analytical solution. (d) Surface tension tensor component $\sigma^{st}_{\theta\theta}$ for overpressurized and equilibrium bubbles. $\sigma^{st}_{\theta\theta}$ is unaffected by the gas bubble pressure.

interface widths, outside the interfacial region, the simulation results matched the analytical solution well.

To test the model's behavior for an underpressurized condition, a 250 nm bubble with $P = 6$ MPa is considered. The same parameters and initial conditions were used as described for the overpressurized bubble, except that $c_g^{b,i} = 0.02413$ and $c_v^{b,i} = 0.97587$ to produce 6 MPa gas pressure. The stress tensor component σ_{rr} is shown in Figure 11b. In this case, $\sigma_{rr} > 0$ outside the bubble, corresponding to a tensile stress in the radial direction in the fuel matrix surrounding the bubble, as expected for an underpressurized bubble. Again, the simulation results converge to the analytical solution as the interface width is decreased, and the simulation results matched the analytical solution well outside the interfacial region.

The presence of elastic energy in the interfacial region has been shown to affect the equilibrium order parameter profile for some elastic energy interpolation schemes in phase-field models, including the Voigt-Taylor scheme used here [42]. Because the surface tension is a function of the order parameter by Equation (50), changes in the order parameter would affect the surface tension; thus, it is important to quantify any changes in the order parameter profile caused by under- or overpressurized bubbles. To evaluate this effect, we evolved an overpressurized bubble with $P = 15$ MPa and $2\lambda = 50$ nm to $t = 10^6$ s to ensure the interfacial profile had reached the equilibrium shape, with vacancy and gas atom source and sink terms set to zero so interfacial position would remain constant. The resulting interfacial profile is shown in Figure 11c, along with comparison to the analytical solution from Equation (66), which is derived in the absence of elastic energy in the interface [31]. As can be seen, the order parameter profile for the overpressurized bubble is in good agreement with the analytical solution. This is in contrast to the results observed in Reference [42], which considered the effect of a misfitting solid precipitate in a matrix; in that case the interface width was decreased compared with the analytical solution. Here, the significantly lower stresses induced by the overpressurized fission gas bubbles compared with the misfitting precipitates, combined with the low stiffness assumed in the bubble phase, result is significantly lower elastic energy in the interfacial region; therefore, the order parameter profile is not significantly affected here. Since the surface tension is a function of the order parameter, the surface tension is also unaffected by the bubble pressure, as demonstrated by Figure 11d, which shows the surface tension tensor component $\sigma^{st}_{\theta\theta}$ for an overpressurized bubble and an equilibrium bubble (again evolved to $t = 10^6$ s with source and sink terms set to zero). The profiles do not differ significantly from each other. The same results were obtained for the other tangential component of surface tension $\sigma^{st}_{\phi\phi}$. (It should be noted that prior to HBS formation, intragranular bubbles in UO_2 are much smaller and have much higher gas pressures; therefore, elastic energy in the interfacial region of non-equilibrium intragranular bubbles may have a greater effect on the order parameter profile and surface tension; future work applying the present model to such bubbles should consider this effect.)

3.4 Model Application to Steady-state and Transient Conditions

3.4.1 Bubble growth during steady-state reactor operating conditions

In this section, the growth of a bubble in the HBS region during typical steady-state reactor operating conditions is simulated. An initial bubble radius of $R = 500$ nm is considered, with an initial pressure of 100 MPa based on observed dislocation punching [6]. The simulation parameters and initial conditions were as described in Section 3.3.1, with $2\lambda = 50$ nm and $c_g^{b,i} = 0.2253$ and $c_v^{b,i} = 0.7747$. The simulation domain size is 1075 nm, corresponding to an initial porosity of 10%. The simulation temperature was 700 K.

The bubble radius and pressure during growth are shown in Figure 12. The rate of growth in the radius slows as the bubble's size increases, as expected due to the constant gas source term in the surrounding fuel matrix. Due to the current burnup limit of 62 GWd/MTU for the peak power rod in commercial LWRs, the rod containing such a bubble would likely be removed from operation before the final simulation time of 10^7 s is reached. Bubble pressure as a function of time is shown in Figure 12b. In this figure, the equilibrium pressure for a bubble with the radius taken from Figure 12a is also plotted. The bubble pressure decreases as growth occurs due to the overpressure-driven influx of vacancies, and comes closer to the equilibrium pressure for the given radius. However, the actual bubble pressure remains above equilibrium throughout the simulation time. Therefore, bubbles in the HBS region that are initially overpressurized are likely to remain significantly above equilibrium pressure for the remainder of their time in the reactor. This increases the risk of rapid pressure increases experienced during a LOCA transient.

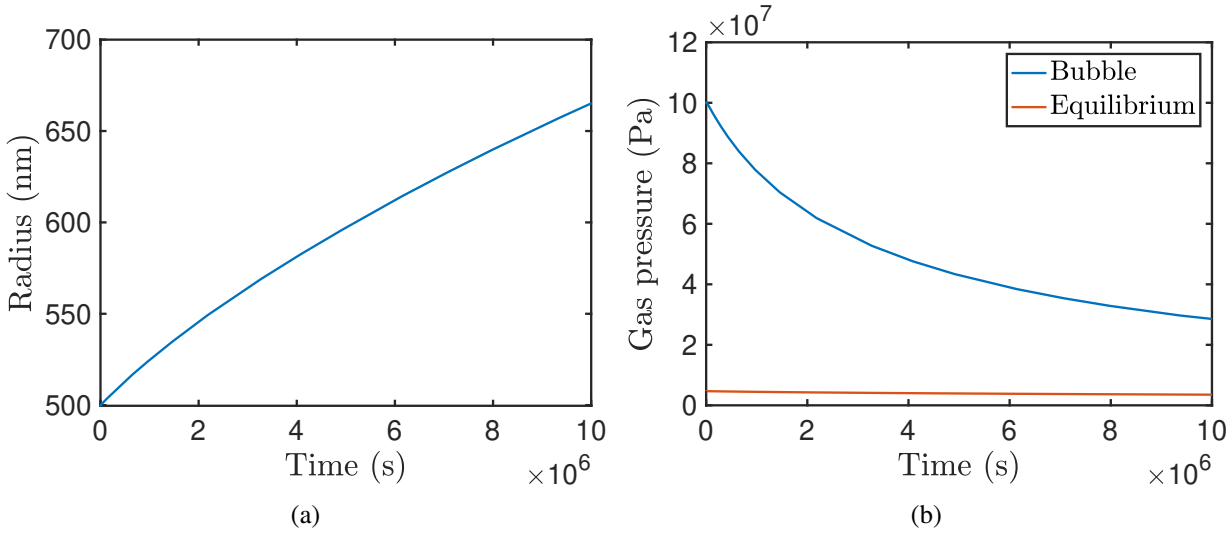

Figure 12: Growth of a bubble in the HBS region during steady-state reactor operating conditions. (a) Radius as a function of time; (b) simulated bubble pressure, and equilibrium pressure for a bubble with radius from (a), as a function of time.

3.4.2 3D simulations of impingement of growing bubbles in the HBS region

To demonstrate the model's capability to capture complex morphological evolution, the growth and impingement of two adjacent bubbles in the HBS region are simulated in 3D. The initial conditions were two bubbles with initial radii of 300 nm and initial pressure of 100 MPa, placed with the bubble centers 800 nm apart. Simulation parameters and initial conditions for the order parameter and composition fields were as described in Section 3.3.1, with $c_g^{b,i} = 0.2253$ and $c_v^{b,i} = 0.7747$, $2\lambda = 100$ nm, and simulation temperature of 700 K. The simulation domain was 3600 nm × 2400 nm × 2400 nm in the x, y, and z directions. Mesh adaptivity was used, with the finest resolution $\Delta x = 2\lambda/4 = 25$ nm used at the interface between the bubble and matrix phase, increasing to $\Delta x = 50$ and 100 nm progressively farther from the interface. Natural boundary conditions were used for all simulation variables. The simulations were run on two nodes of the Falcon cluster at INL with 36 cores/node and required approximately 90 hours to reach a simulation time of 2×10^7 s, demonstrating that, in spite of the complexity of the model, its computational requirements are not excessive.

The results of the simulations are shown in Figure 13. The morphology of the bubbles (as defined by the isosurface of $\eta = 0.5$) is shown as the bubbles grow and coalesce in (a), (c), (e), and (g). The hydrostatic stress state in the matrix surrounding the bubbles is shown on the plane defined by $z = 1200$ nm (which is at the center of the domain in the z-direction) in (b), (d), (f), and (h). The plane is colored by the local hydrostatic stress at each position, and the bubble morphology in grey remains in the images.

The initial bubble morphology and stress state is shown in Figures 13a and 13b (these are shown at $t = 10.4$ s rather than $t = 0$, since a short amount of time is required for interfacial profiles to locally equilibrate). At the beginning of the simulation, the bubbles are significantly overpressurized as set in the initial conditions. This results in a compressive (negative) hydrostatic stress in the matrix immediately outside the bubbles, which decreases to a value near zero within approximately 100 nm of the interface. Just after the bubbles coalesce, a region of enhanced compressive hydrostatic stress appears (see Figure 13d) surrounding the neck region where the bubbles have coalesced. This acts as an additional driving force for vacancy flux due to the vacancy eigenstrain. As bubble growth proceeds, the neck region grows outwards along with the

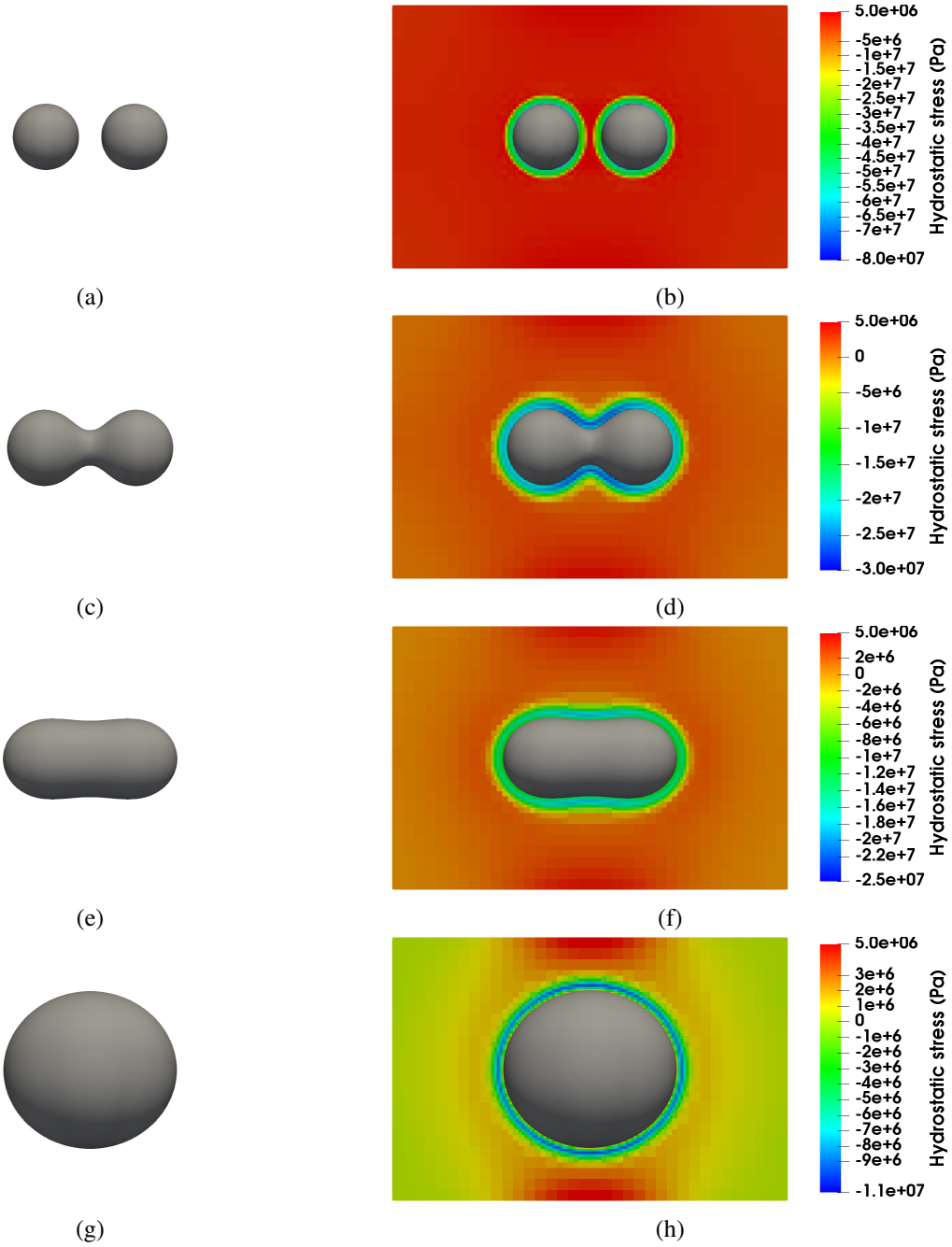

Figure 13: Growth and impingement of two bubbles in the HBS region during steady-state reactor operating conditions. (a), (c), (e), and (g) show the bubble morphology as defined by the isosurface of $\eta = 0.5$. (b), (d), (f), and (h) show the hydrostatic stress at the center of the simulation domain, visualized as mapped on the plane $z = 1200$ nm, with the grey isosurfaces of the bubble morphology remaining. Simulation times: (a), (b): $t = 10.4$ s; (c), (d): $t = 1.6 \times 10^6$ s; (e), (f): $t = 4.2 \times 10^6$ s; (g), (h): $t = 2.2 \times 10^7$ s. (Note that the minimum of the color bar in each subfigure has been adjusted to allow resolution of finer details in the the stress distribution.)

bubble edges, resulting in a pill-shaped morphology, as shown in Figures 13e and 13f, at $t = 4.2 \times 10^6$ s. Finally, at a much later simulation time of $t = 2.2 \times 10^7$ s, the bubble morphology approaches the expected spherical shape, as shown in Figure 13g. At this time, the magnitude of the hydrostatic stress surrounding the bubble is much lower, as the gas pressure within the bubble has been reduced but has not yet reached the equilibrium pressure, as was observed in Figure 12b. (There is also a region of slight enhancement of the hydrostatic stress near the top and bottom of the center of the simulation domain, which is a result of the decaying stress field interacting with the simulation domain boundaries in the traction-free boundary condition.)

3.4.3 LOCA pressure transients

During a LOCA, temperature increases rapidly in the fuel, at a rate on the order of 5 K/s [2]. Temperatures may reach as high as 1400 K before a quench can be initiated. In this section, we investigate how the sudden temperature increase of a typical LOCA transient affects the overpressurized bubbles found in the HBS region in order to determine whether there is any significant change in bubble size, and to determine the bubble pressure in response to the transient for various bubble parameters.

A series of simulations was performed at an initial bubble temperature of 700 K. Temperature was ramped at 5 K/s for a total of 140 s, resulting in a final temperature of 1400 K. Simulations with varying bubble radius, initial pressure (at fixed bubble radius), and external pressure boundary condition (at fixed bubble radius) were performed, with $2\lambda = 50$ nm. Prior to the beginning of the transient, the bubble evolution model described in Section 3.4.1 was run, starting from a radius slightly below the nominal radius given for each simulation, to allow order parameter and concentration fields to fully equilibrate prior to the LOCA transient. The transient was initiated when the radius (as determined by the position where $\eta = 0.5$) exactly matched the nominal radius.

Simulations with varying initial gas pressure were conducted for a bubble with a constant radius of $R = 250$ nm. A gas pressure of 200 MPa is estimated to be an upper bound for the pressure of a bubble of this size, based on the dislocation punching pressure for a bubble of this size [6]. If the bubble pressure was above this value, dislocations would be punched out in the surrounding fuel matrix, causing the bubble to grow. However, pressures could be lower than this upper bound estimate. To investigate the effect of varying the initial pressure P_0, simulations with initial bubble pressures of 50, 100, and 200 MPa were conducted. In each case, the radius of the bubble did not change significantly during the LOCA transient. The resulting pressures are shown in Figure 14a. Because the radius of the bubble remains constant during the transient, pressure increases linearly as a function of time with temperature, as expected from the van der Waals equation of state with constant density.

Although the bubble size in these simulations did not change during LOCA transients, one potential factor that could affect this conclusion is the enhanced diffusivity of defects along grain boundaries, which could be as much as 10^6 times greater than bulk diffusivities for normal thermally activated diffusion [52]. Although the diffusivities of vacancies and Xe atoms along UO_2 grain boundaries in radiation-enhanced conditions have not been determined to our knowledge, and the present model does not include grain boundaries explicitly, we have assessed the potential impact of enhanced diffusivities along grain boundaries on bubble growth during transients using the following methodology. The diffusivity along grain boundaries is expected to be much higher than in the bulk; however, the volume of the grain boundary regions is significantly smaller than the bulk of the grains. To represent in an averaged way the potentially increased diffusivities along the grain boundaries in our 1D simulation domain, we assume the grain boundary region is no more than 1% of the total volume of the fuel matrix region, and set the diffusivities of the vacancies and gas atoms in the fuel matrix to 10^4 of their original bulk values, based on 1% of an increase of 10^6. The diffusivities of the defects in the gas bubble were increased by the same factor to ensure that they remain significantly greater than the diffusivities in the solid, as is expected physically. The LOCA transient simulation of a 250

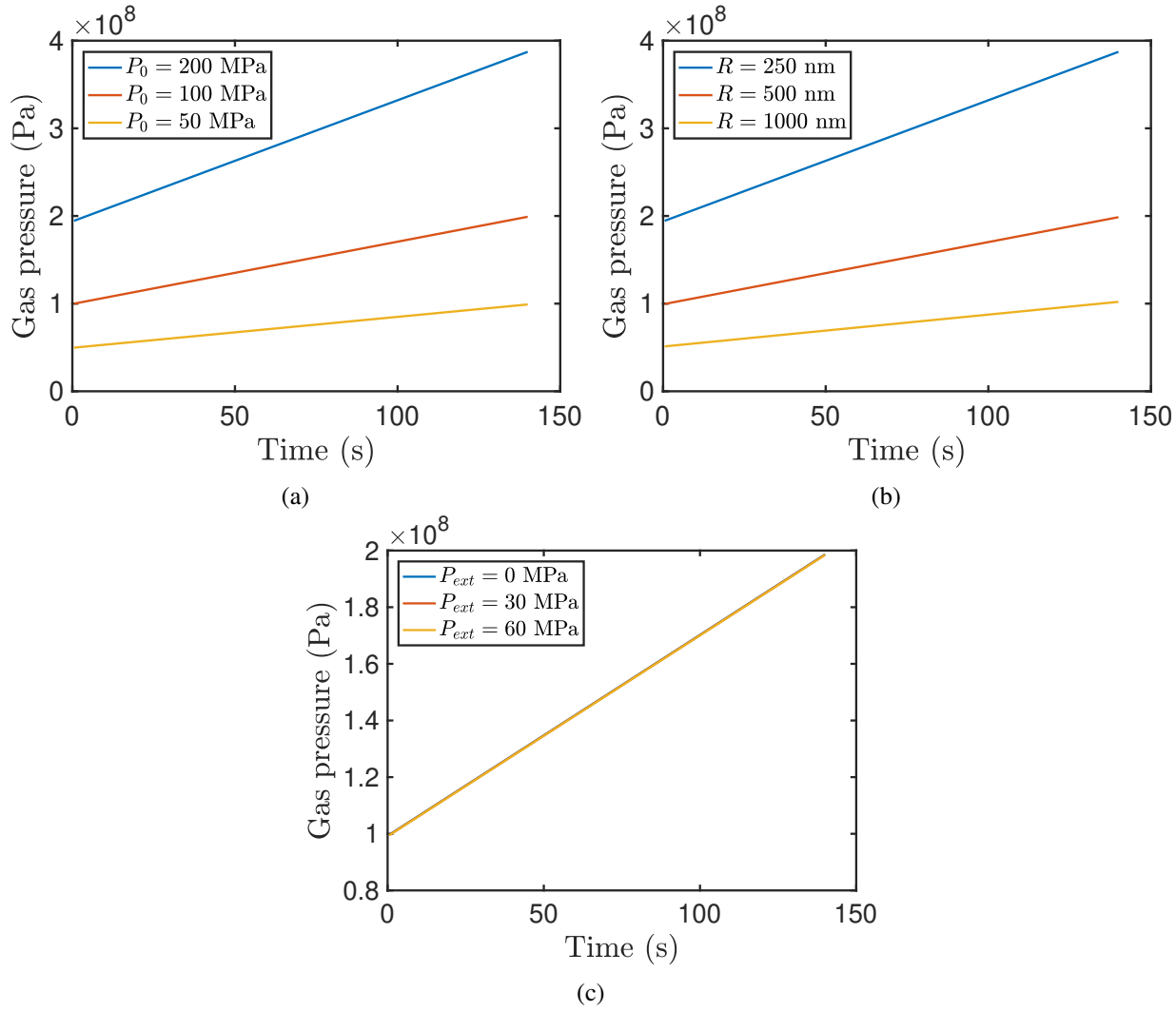

Figure 14: (a) Pressure as a function of time for a bubble with $R = 250$ nm and varying initial bubble pressure. The upper bound estimate for initial bubble pressure is 200 MPa. (b) Bubble pressure as a function of time for varying bubble radius, with pressures determined by a lower bound estimate. (c) Bubble pressure as a function of time for varying P_{ext}.

nm radius bubble with an initial pressure of 200 MPa was repeated with the increased diffusivities. Even with the increased diffusivities, there was no significant change in bubble size during the transient. Based on these results, we conclude that, even if the defect diffusivities along grain boundaries are significantly higher than the radiation-enhanced bulk values, bubble size should not change significantly during a typical LOCA transient. If accurate values for defect diffusivities along grain boundaries become available in the future, their impact may be reassessed using a realistic representation of the grain boundary structure with 3D simulations.

Simulations of bubbles with varying radii were also conducted. R = 250, 500, and 1000 nm were considered. The pressures for these bubbles were set at 200, 100, and 50 MPa, respectively, based on upper bound estimates from dislocation punching [6]. The pressures for these bubbles are shown in Figure 14b. As expected based on the previous results, the bubble radius did not change significantly during the transient, and the bubble pressure therefore increased linearly with temperature.

Finally, the pressure at the external boundary at the edge of the domain, P_{ext}, was varied for a bubble with a radius of $R = 500$ nm. In addition to the previously simulated $P_{ext} = 0$, $P_{ext} = 30$, and 60 MPa were considered. The bubble radii again did not change significantly, and the external restraint pressure did not significantly affect the pressure transient. The external pressure may have a more significant effect on the fracture behavior in the surrounding matrix, which will be considered further in Section 4.

3.5 Conclusions

In this work, a new phase-field model of fission gas bubble evolution in nuclear fuel has been developed and parameterized for UO_2. The model includes the effects of the gas pressure inside the bubble and the surface tension of the bubble-matrix interface, accounting for the opposing effects of these factors on the stress state of the fuel and resulting microstructural evolution. The model was shown to give the expected stress state in the fuel matrix surrounding a bubble for equilibrium, overpressurized, and underpressurized bubbles.

The model was applied to simulate growth of initially overpressurized bubbles in the HBS region during steady-state growth conditions. During growth of a single isolated bubble, the pressure decreases as growth proceeds, but remains overpressurized during the remainder of the the fuel lifetime in the reactor. During growth and impingement of two nearby bubbles, the model captured the complex morphological evolution and the effect of the stress state on growth. Following impingement of the two bubbles, the combined bubble remained overpressurized.

To improve understanding of the response of fuel in the HBS region to LOCA conditions, the response of a single bubble in the HBS region to a temperature transient typical of LOCA conditions was simulated. The size of the bubble did not change significantly during the transient for a variety of initial conditions, including varying bubble size, initial pressure, and external restraint pressure. It was also shown that enhanced defect diffusivities along grain boundaries is not likely to result in bubble size change during transients. This demonstrates that future work using a phase-field fracture model to investigate fracture in response to LOCA transients does not need to account for a change in bubble size, thus simplifying the model required for that work. The calculated pressure transients from Section 3.4.3 will also be used as input to the phase-field fracture model. It is expected that the insights gained from this work will contribute to an improved understanding of the mechanism of fuel pulverization, an improved capability to predict its occurrence, and the development of strategies to mitigate its impact, potentially leading to increases in burnup limits and improved economics for commercial LWRs.

4 PHASE FIELD MODELING OF UO_2 HBS FRAGMENTATION

4.1 Phase Field Fracture Model

The mechanics minimization problem is regularized and approximated using the phase-field c as per:

$$\{\boldsymbol{u}, c\} = \arg\min_{\boldsymbol{u},c} \Psi(\boldsymbol{u}, \boldsymbol{\nabla u}, c, \boldsymbol{\nabla} c), \tag{69a}$$

$$\text{subject to} \qquad \boldsymbol{u} = \boldsymbol{g}, \quad \forall \boldsymbol{x} \in \partial\Omega_D, \tag{69b}$$

$$\dot{c} \geqslant 0, \quad \forall \boldsymbol{x} \in \Omega \tag{69c}$$

where (69c) is the irreversibility condition equivalent to the "no healing" condition on the permanent crack set and:

$$\begin{aligned}\Psi(\boldsymbol{u}, \boldsymbol{\nabla u}, c, \boldsymbol{\nabla} c) =& \Psi_{\text{elastic}}(\boldsymbol{\nabla u}, g(c)) + \Psi^{l}_{\text{fracture}}(c, \boldsymbol{\nabla} c) - \Psi_{\text{dissipation}}(c) \\ &- \Psi^{\text{traction}}_{\text{external}}(\boldsymbol{u}) - \widetilde{\Psi}^{\text{pressure}}_{\text{external}}(\boldsymbol{u}, c, \boldsymbol{\nabla} c),\end{aligned} \tag{70a}$$

$$\Psi_{\text{elastic}}(\boldsymbol{\nabla u}, g(c)) = \int_{\Omega} g(c)\psi^{\langle \text{A} \rangle}_{\text{elastic}}(\boldsymbol{\nabla u})\, \mathrm{d}V + \int_{\Omega} \psi^{\langle \text{I} \rangle}_{\text{elastic}}(\boldsymbol{\nabla u})\, \mathrm{d}V, \tag{70b}$$

$$\Psi^{l}_{\text{fracture}}(c, \boldsymbol{\nabla} c) = \int_{\Omega} \mathcal{G}_c \gamma_l(c, \boldsymbol{\nabla} c)\, \mathrm{d}V, \tag{70c}$$

$$\dot{\Psi}_{\text{dissipation}}(\dot{c}) = \int_{\Omega} \frac{1}{2}\eta \dot{c}^2\, \mathrm{d}V, \tag{70d}$$

$$\Psi^{\text{traction}}_{\text{external}}(\boldsymbol{u}) = \int_{\partial\Omega_N} \boldsymbol{\tau} \cdot \boldsymbol{u}\, \mathrm{d}A, \tag{70e}$$

$$\widetilde{\Psi}^{\text{pressure}}_{\text{external}}(\boldsymbol{u}, c, \boldsymbol{\nabla} c) = -\int_{\Omega} p \boldsymbol{\nabla} c \cdot \boldsymbol{u} I'(c)\, \mathrm{d}V \tag{70f}$$

Let us define trial spaces:

$$\mathcal{U} = \left\{ \boldsymbol{u} | \boldsymbol{u} \in \mathcal{H}^1(\Omega)^d, \boldsymbol{u} = \boldsymbol{g}, \forall \boldsymbol{x} \in \partial\Omega \right\}, \quad \mathcal{C} = \left\{ c | c \in \mathcal{H}^1(\Omega), \dot{c} \geqslant 0, \forall \boldsymbol{x} \in \Omega \right\} \tag{71}$$

along with their corresponding weighting spaces:

$$\mathcal{V} = \left\{ \delta\boldsymbol{u} | \delta\boldsymbol{u} \in \mathcal{H}^1(\Omega)^d, \boldsymbol{u} = \boldsymbol{0}, \forall \boldsymbol{x} \in \partial\Omega \right\}, \quad \mathcal{Q} = \left\{ \delta c | \delta c \in \mathcal{H}^1(\Omega), \delta c \geqslant 0, \forall \boldsymbol{x} \in \Omega \right\} \tag{72}$$

The optimality conditions for $\boldsymbol{u}$ follow from the functional derivative of the objective function Ψ as per:

$$\begin{aligned}&\int_{\Omega} \boldsymbol{\nabla} \cdot \frac{\partial \psi_{\text{elastic}}(\boldsymbol{\nabla u}, g(c))}{\partial \boldsymbol{\nabla u}}\, \mathrm{d}V - \int_{\partial\Omega_N} \frac{\partial \psi_{\text{elastic}}(\boldsymbol{\nabla u}, g(c))}{\partial \boldsymbol{\nabla u}} \boldsymbol{n}\, \mathrm{d}A \\ &+ \int_{\partial\Omega_N} \frac{\partial \psi^{\text{traction}}_{\text{external}}(\boldsymbol{u})}{\partial \boldsymbol{u}}\, \mathrm{d}A + \int_{\Omega} \frac{\partial \widetilde{\psi}^{\text{pressure}}_{\text{external}}(\boldsymbol{u}, c, \boldsymbol{\nabla} c)}{\partial \boldsymbol{u}}\, \mathrm{d}V = 0, \quad \forall \Omega' \subseteq \Omega, \forall \partial\Omega'_N \subseteq \partial\Omega_N\end{aligned} \tag{73}$$

Substituting (70) yields:

$$\boldsymbol{\nabla} \cdot \boldsymbol{\sigma} - pI'(c)\boldsymbol{\nabla} c = \boldsymbol{0}, \quad \forall \boldsymbol{x} \in \Omega, \tag{74a}$$

$$\boldsymbol{\sigma n} = \boldsymbol{\tau}, \quad \forall \boldsymbol{x} \in \Omega_N \tag{74b}$$

where $\boldsymbol{\sigma} = \dfrac{\partial \psi_{\text{elastic}}}{\partial \boldsymbol{\nabla u}}$ is the stress-strain constitutive relation. The optimality conditions for c that are subject to the irreversibility constraint (69c) also follow from the functional derivative (with respect to the rate of the objective function) and recover the Karush–Kuhn–Tucker (KKT) conditions:

$$\begin{aligned}
&\int_\Omega \frac{\partial \psi_{\text{elastic}}(\boldsymbol{\nabla u}, g(c))}{\partial c}\dot{c}\,\mathrm{d}V - \int_\Omega \boldsymbol{\nabla}\cdot\frac{\partial \psi^l_{\text{fracture}}(c,\boldsymbol{\nabla} c)}{\partial \boldsymbol{\nabla} c}\dot{c}\,\mathrm{d}V + \int_{\partial\Omega}\frac{\partial \psi^l_{\text{fracture}}(c,\boldsymbol{\nabla} c)}{\partial \boldsymbol{\nabla} c}\cdot\boldsymbol{n}\dot{c}\,\mathrm{d}A \\
&+\int_\Omega \frac{\partial \psi^l_{\text{fracture}}(c,\boldsymbol{\nabla} c)}{\partial c}\dot{c}\,\mathrm{d}V + \int_\Omega \boldsymbol{\nabla}\cdot\frac{\partial \widetilde{\psi}^{\text{pressure}}_{\text{external}}(c,\boldsymbol{\nabla} c)}{\partial \boldsymbol{\nabla} c}\dot{c}\,\mathrm{d}V - \int_{\partial\Omega}\frac{\partial \widetilde{\psi}^{\text{pressure}}_{\text{external}}(c,\boldsymbol{\nabla} c)}{\partial \boldsymbol{\nabla} c}\cdot\boldsymbol{n}\dot{c}\,\mathrm{d}A \\
&+\int_\Omega \frac{\partial \widetilde{\psi}^{\text{pressure}}_{\text{external}}(c,\boldsymbol{\nabla} c)}{\partial c}\dot{c}\,\mathrm{d}V + \int_\Omega \frac{\partial \dot{\psi}_{\text{dissipation}}(\dot{c})}{\partial \dot{c}}\dot{c}\,\mathrm{d}V = 0, \quad \forall\Omega'\subseteq\Omega, \forall\partial\Omega'_N\subseteq\partial\Omega_N
\end{aligned} \tag{75}$$

Again, substituting (70) yields:

$$\begin{aligned}
&\phi^f \geqslant 0, \quad \dot{c}\geqslant 0, \quad \phi^f\dot{c} = 0, \\
&\text{with } \phi^f = \begin{cases} \eta\dot{c} - \boldsymbol{\nabla}\cdot\boldsymbol{\xi} + \dfrac{\mathcal{G}_c}{c_0 l}\alpha'(c) - Y, & \forall \boldsymbol{x}\in\Omega, \\ \boldsymbol{\xi}\cdot\boldsymbol{n} + pI'(c)\boldsymbol{u}\cdot\boldsymbol{n}, & \forall\boldsymbol{x}\in\partial\Omega \end{cases}
\end{aligned} \tag{76}$$

where $\boldsymbol{\xi} = \dfrac{\partial \psi^l_{\text{fracture}}}{\partial \boldsymbol{\nabla} c} = \dfrac{2\mathcal{G}_c l}{c_0}\boldsymbol{\nabla} c$ is the thermodynamic conjugate to $\boldsymbol{\nabla} c$, and Y is the generalized fracture driving force consisting of contributions from the active elastic energy density as well as work done by pressure:

$$Y = -g'(c)\psi^{\langle \mathrm{A}\rangle}_{\text{elastic}} + pI'(c)\boldsymbol{\nabla}\cdot\boldsymbol{u} \tag{77}$$

With a view towards the solution strategy, using a variational inequality solver (e.g., a primal-dual active set algorithm) to enforce the irreversibility constraint requires discretization of the fracture envelope ϕ^f only on the inactive set $\dot{c} > 0$ and $\phi^f = 0$. Hence, only the weak form in the case of $\phi^f = 0$ is outlined below:

Given $\boldsymbol{g}$, $\boldsymbol{\tau}$, and c_0, find $\boldsymbol{u}\in\mathcal{U}$ and $c\in C$, such that $\forall\delta\boldsymbol{u}\in\mathcal{V}$ and $\forall\delta c\in\mathcal{Q}$:

$$\int_\Omega \boldsymbol{\sigma} : \boldsymbol{\nabla}\delta\boldsymbol{u}\,\mathrm{d}V + \int_\Omega pI'(c)\boldsymbol{\nabla} c\cdot\delta\boldsymbol{u}\,\mathrm{d}V - \int_{\partial\Omega_N}\boldsymbol{\tau}\cdot\delta\boldsymbol{u}\,\mathrm{d}A = 0, \tag{78a}$$

$$\int_\Omega \eta\dot{c}\delta c\,\mathrm{d}V + \int_\Omega \boldsymbol{\xi}\cdot\boldsymbol{\nabla}\delta c\,\mathrm{d}V + \int_\Omega \frac{\mathcal{G}_c}{c_0 l}\alpha'(c)\delta c\,\mathrm{d}V - \int_\Omega Y\delta c\,\mathrm{d}V + \int_{\partial\Omega} pI'(c)\boldsymbol{u}\cdot\boldsymbol{n}\delta c\,\mathrm{d}A = 0 \tag{78b}$$

4.2 Verification

4.2.1 Pressurized crack propagation

We considered a pressurized crack propagation problem conducted by [53]. This problem serves to verify whether cracks should begin to grow once a critical pressure loading is applied. In Figure 15d, an initial crack is prescribed in the center with a length of $2a$. As seen in Figure 15a, the phase-field variable c is initialized to be 1.0 only for those nodes on the bottom boundary belonging to the crack. After the first time

step, the phase-field variable c will be regularized to a correct profile, as shown in Fig 15b. This differs from the others' approach [53, 54], which involved imposing initial values for a set of elements. Due to symmetry, only half the domain with a size of $L \times L/2$ is used as shown in Figure 15c. The ratio L/a is taken to be 20. The displacements on all outer boundaries are set to zero. A uniform pressure is increased until the crack begins to propagate. The propagation of the crack at fixed pressure conditions is unstable. According to the linear elastic fracture mechanics (LEFM), the normalized critical pressure is given as:

$$\frac{p_c}{\sigma_0} = \sqrt{\frac{l}{\pi a}} \tag{79}$$

where $\sigma_0 = \sqrt{E/(1-\nu^2)\mathcal{G}_c^{\text{eff}}/l}$. The $\mathcal{G}_c^{\text{eff}}$ is the effective fracture toughness in the phase-field fracture model and is given as [55, 54]:

$$\mathcal{G}_c^{\text{eff}} = \mathcal{G}_c \left(\frac{h}{4c_0 l} + 1 \right) \tag{80}$$

The LEFM solution is based on a brittle fracture model in which critical fracture stress approaches an infinite value. A comparison between the numerical results and the LEFM solution for the critical pressure values is shown in Figure 16. The phase-field solution converges as σ_c increases and shows good agreement with the LEFM solution.

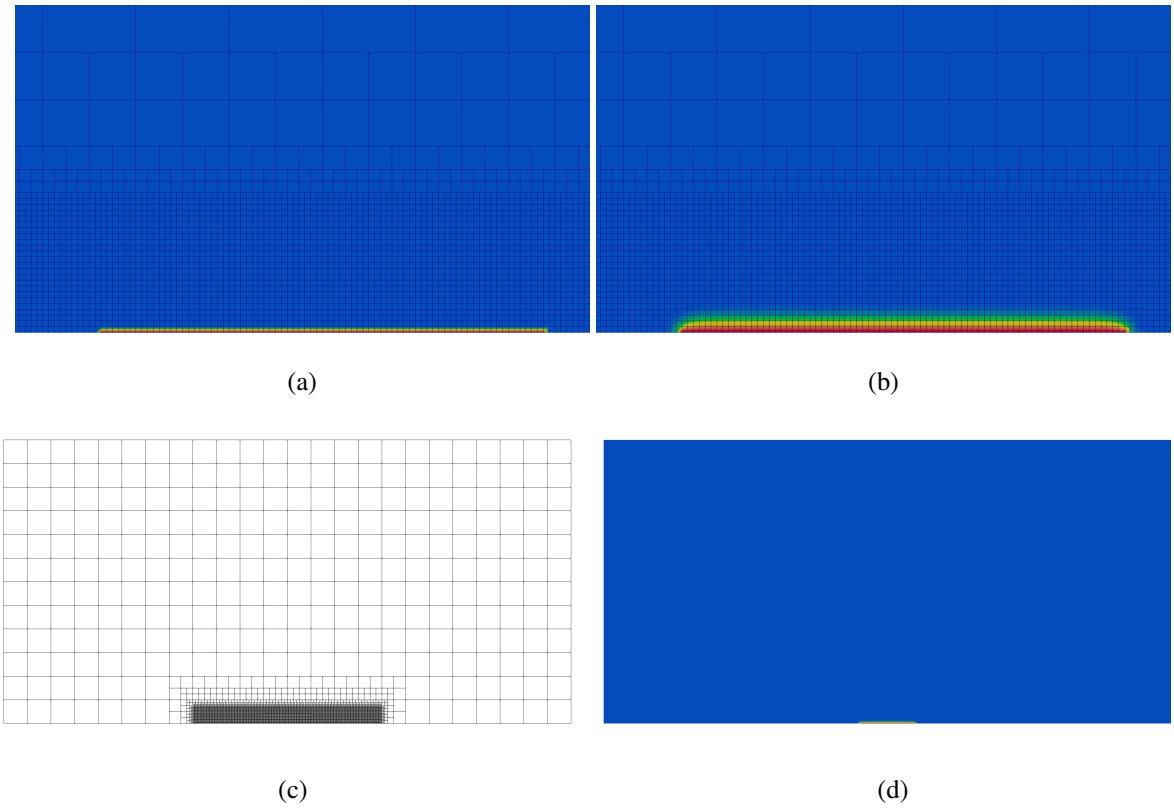

(a) (b) (c) (d)

Figure 15: Pressurized crack propagation problem: (a) Initial values are imposed on crack surface nodes (zoomed view). (b) Regularized phase-field variable after one time step (zoomed view). (c) Mesh with five levels of local refinement. (d) Preexisting crack. The red and blue color correspond to value of 1.0 and 0, respectively.

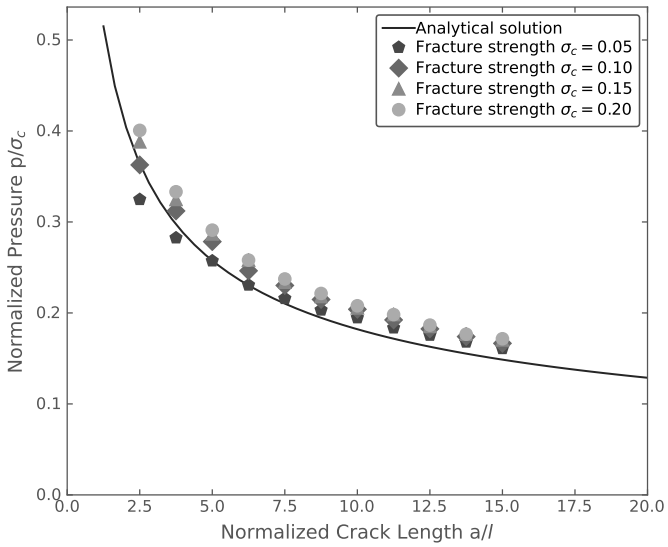

Figure 16: Comparison between the numerical results and the LEFM solution for the critical pressure values.

4.3 Application: High-burnup Fragmentation

We further simulated fission-gas-induced inter-granular fracture of UO_2 HBS. The material properties and model parameters are summarized in Table 3. The fracture stress of UO_2 was taken to be 130 MPa [56]. Due to a lack of experimental data, the energy release rate $\mathcal{G}_c^{\mathrm{GB}}$ was assumed to be 0.0012 Pa·m and the Griffith's characteristic length $l_{ch} = E\mathcal{G}_c/\sigma_c^2 \approx 22.78$ nm.

To facilitate inter-granular crack propagation, the energy release rate of grain interiors must satisfy the following:

$$\mathcal{G}_c^{\mathrm{INT}} \gg \mathcal{G}_c^{\mathrm{GB}} \tag{81}$$

so that crack propagation is predominately driven by inter-granular elastic energy. In this work, the poly-crystalline microstructure is described by a set of non-conserved field variables obtained from a phase-field grain growth model [24]. The initial grain centroids are generated from a random close-packing Voronoi structure[57] that provides equiaxed grains with average radius of 85 nm. The field variable ϕ_i equals 1 within the ith grain and 0 elsewhere. Regions where ϕ_i varies between 0 and 1 correspond to grain boundaries. The grain boundaries are computed as $bnd = \sum \phi_i^2$. If bnd is less than the cut-off value, $\mathcal{G}_c$ is given by $\mathcal{G}_c^{\mathrm{GB}}$. Otherwise, $\mathcal{G}_c$ is given by $\mathcal{G}_c^{\mathrm{INT}}$. For simulations considered in this work, a cut-off value of 0.75 was observed to be appropriate.

In this work, the elastic properties of the grain interiors are assumed to be isotropic and therefore do not depend on crystal orientations. Similarly, a field variable is used to represent bubbles in a diffusive manner. A Young's modulus of $E = 385$ GPa and a Poisson's ratio of $\nu = 0.23$—typical for UO_2 [58]—were assigned to the bulk, while a very small Young's modulus of $E_b = 10^{-9}E$ was assigned to the bubbles to remove zero-energy modes. Hydrostatic pressure was applied to the bubble phase. When cracks occurred, the same pressure was applied on the crack surfaces. Symmetry boundary conditions were applied to the bottom and left boundaries.

Table 3: Parameters used to perform the UO_2 simulation.

Property	Symbol	Value	Unit	Reference
Young's modulus	E	385	GPa	[58]
Fracture stress	σ_c	130	MPa	[56]
Energy release rate of the grain boundary	$\mathcal{G}_c^{\mathrm{GB}}$	0.0012	Pa·m	Lack of experiment data
Energy release rate of the grain	$\mathcal{G}_c^{\mathrm{INT}}$	0.012	Pa·m	Equation 81
Length scale	l	0.01	μm	Equation 55
Viscosity	η	1×10^{-3}	s·mm^{-1}	[59, 60]

4.3.1 LOCA pressure transients

We started to investigate gas-pressure-induced fracture behavior during LOCA-driven temperature transients. During a LOCA transient, temperatures in the fuel rod increase rapidly, leading to increased pressure in the gas contained within the bubbles. The temperature as a function of time at the edge of a representative pellet for each rod was obtained by using the engineering-scale fuel performance code BISON [61] simulation of the Studsvik Rod 196 experiment [62]. The temperature was used as an input to the KKS phase-field model [9] to determine the pressure as a function of time. In the KKS phase-field model, the gas pressure is assumed to be 100 MPa during steady-state reactor operation at 700 K. The Studsvik experiment was begun with a fixed temperature hold at 572.6 K at the outer surface prior to the transient, resulting in the initial pressure at the start of the transient decreasing from 100 MPa to below 80 MPa. The pressure was passed to our phase-field fracture model to simulate fracture in the regions surrounding individual bubbles.

Two radii (0.25 μm and 0.5 μm) were considered. No external loading was applied in these two cases. As shown in Figures 17 and 18, the fracture patterns are different between these two cases. For the case with a smaller bubble, two major cracks formed, both propagating to outer surfaces. For the case with a larger bubble, only one major crack was able to propagate to a free surface, and the propagation of other cracks was suppressed by this major crack. Cracks initiate when tensile stress caused by the pressurized bubble reaches critical fracture strength. The critical pressures are 120.17 and 89.69 MPa for the small and large bubbles, respectively. The critical pressure is lower for the larger bubble because larger bubbles cause higher stress concentrations at the bubble/matrix interface, with the same pressure applied inside a bubble. This indicates bubble size affects the fracture behavior of HBS.

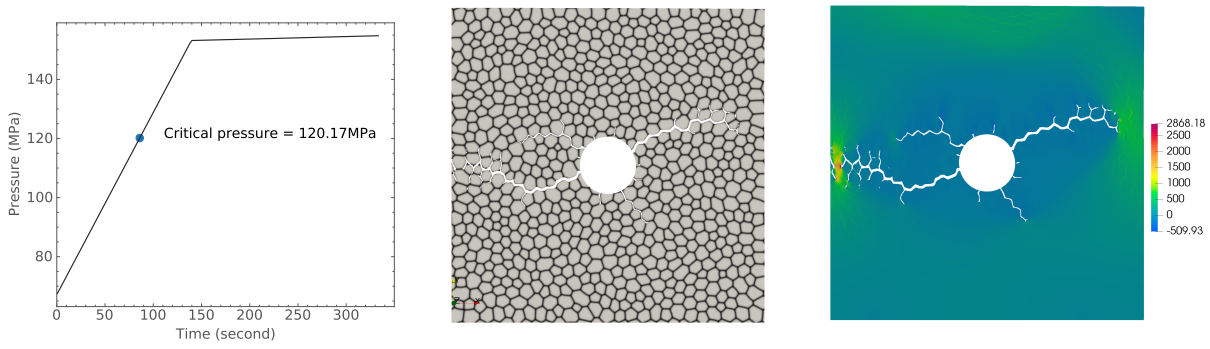

(a) (b) (c)

Figure 17: Radius = 0.25 μm; external pressure = 0 MPa: (a) Pressure history. (b) Cracks propagation. (c) Maximum principal stress.

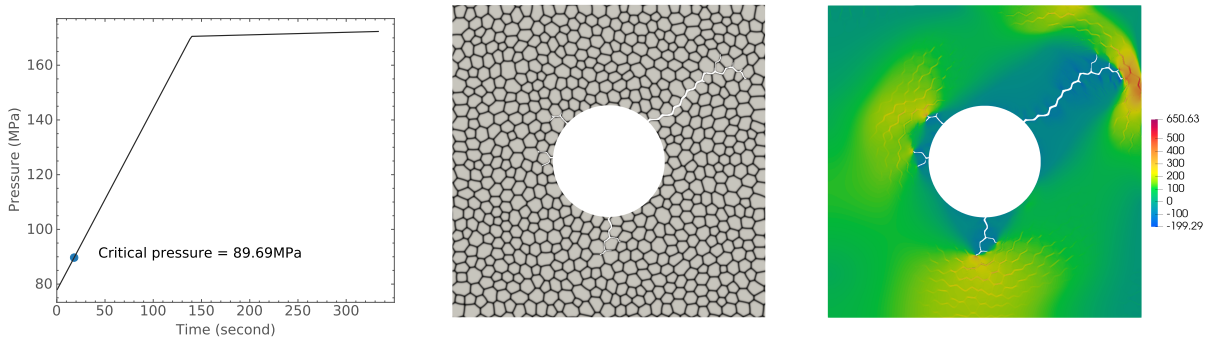

(a) (b) (c)

Figure 18: Radius = 0.5 μm; external pressure = 0 MPa: (a) Pressure history. (b) Crack propagation. (c) Maximum principal stress.

To study the effect of external pressure, different external pressures were then applied on the top and right boundaries. In a fuel pellet, such external pressures can be caused by the fuel-cladding mechanical interaction. The results from using three different external pressures—0, 30, and 60 MPa—are shown in Figures 18, 19, and 20, respectively. The external pressure can alter the critical pressure, as it plays a role in compressing the bubble. The critical pressure becomes significantly higher for larger external pressure values, though the crack pattern does not significantly change.

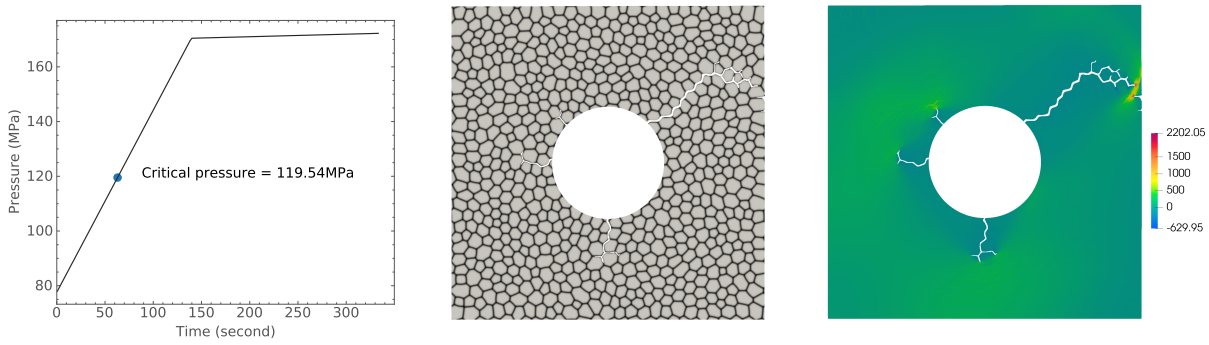

(a) (b) (c)

Figure 19: Radius = 0.5 μm; external pressure = 30 MPa: (a) Pressure history. (b) Crack propagation. (c) Maximum principal stress.

4.3.2 Multi-bubble interaction

We next considered two cases: one with two bubbles and one with three. The bubble radius was 0.25 μm. The centers of the bubbles in the two-bubble case were at (0.4 μm, 1.4 μm) and (1.4 μm, 0.4 μm), whereas the centers of the bubbles in the three-bubble case were at (0.5 μm, 1.6 μm), (1.6 μm, 0.5 μm), and (1.6 μm, 1.6 μm). Figures 21 and 22 show the crack propagation and maximum principal stress contours for the two- and three-bubble cases, respectively. Unlike the one-bubble case in which cracks propagate to a free surface, crack propagation in cases involving multiple bubbles is strongly affected by bubble locations. Cracks prefer to form between those bubbles that are positioned the closest to each other. It is clear connected cracks and

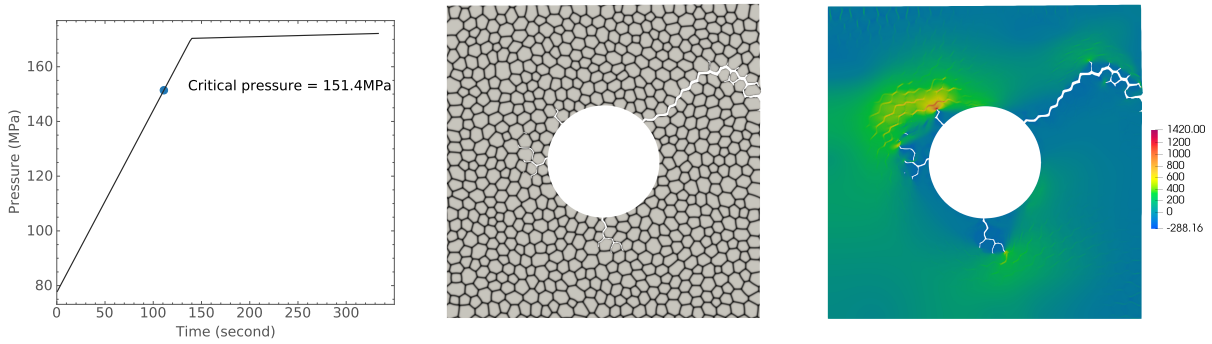

(a) (b) (c)

Figure 20: Radius = 0.5 μm; external pressure = 60 MPa: (a) Pressure history. (b) Crack propagation. (c) Maximum principal stress.

bubbles form a large fragment at the lower-left corner in both Figures 21 and 22. Such fragments consist of multiple grains, and their sizes are determined by the bubble spatial distribution.

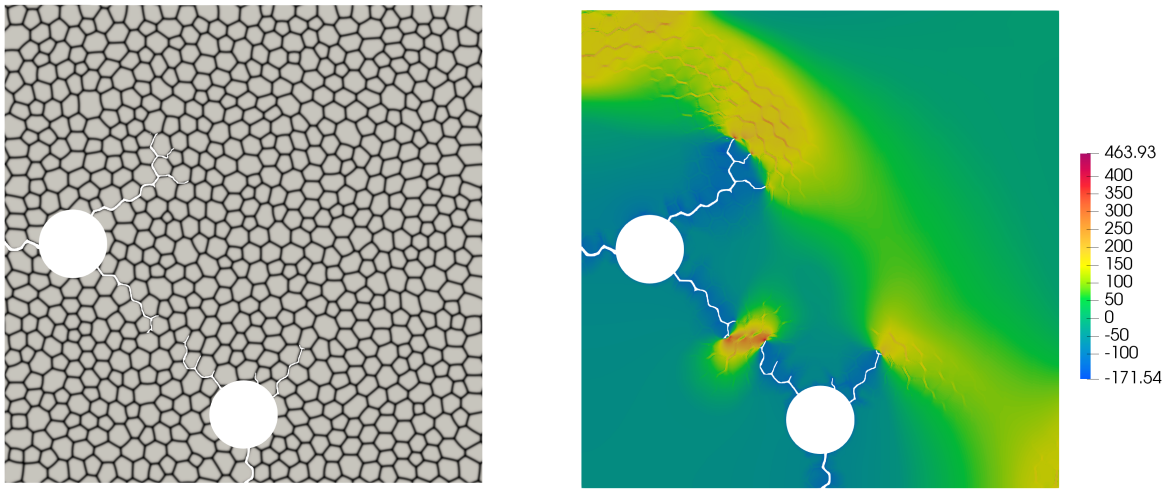

(a) (b)

Figure 21: Two-bubble case: (a) Crack propagation; (b) Maximum principal stress.

4.3.3 Partial HBS

In this section, we use the output from the HBS formation simulations as our initial condition. In this case, the initial condition is generated from the phase field simulations that explicitly model the defect evolution and recrystallization behavior leading to HBS formation. A detailed description of the model can be found in [9]. Considering that fragmentation has been observed in partially recrystallized zones, we focused on the fracture behavior of the partial HBS obtained from these simulations. Three HBS at different recrystallization stages with 25%, 60%, and 100% recrystallization fraction were considered. A linearly increasing pressure was applied. For all three cases, crack initiation occurred at around 60 MPa, thanks to their similar bubble

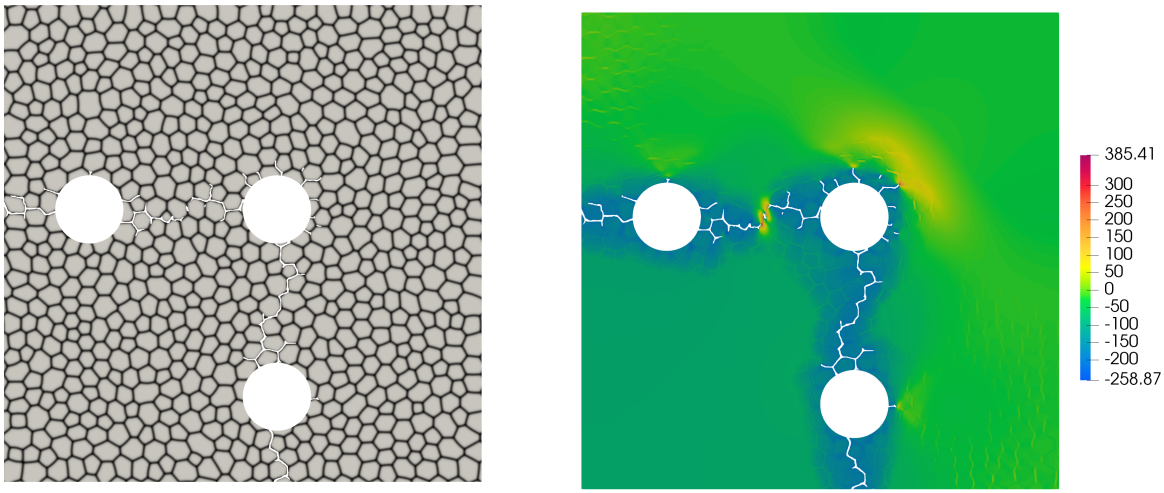

(a) (b)

Figure 22: Three-bubble case: (a) Crack propagation; (b) Maximum principal stress.

sizes. Crack initiation locations varied among the three cases, since more grains form around the bubble during recrystallization and their points of intersection with the bubble can become possible initiation sites. In addition, the recrystallized grain structures change the grain boundary morphology, thus altering crack propagation directions and paths.

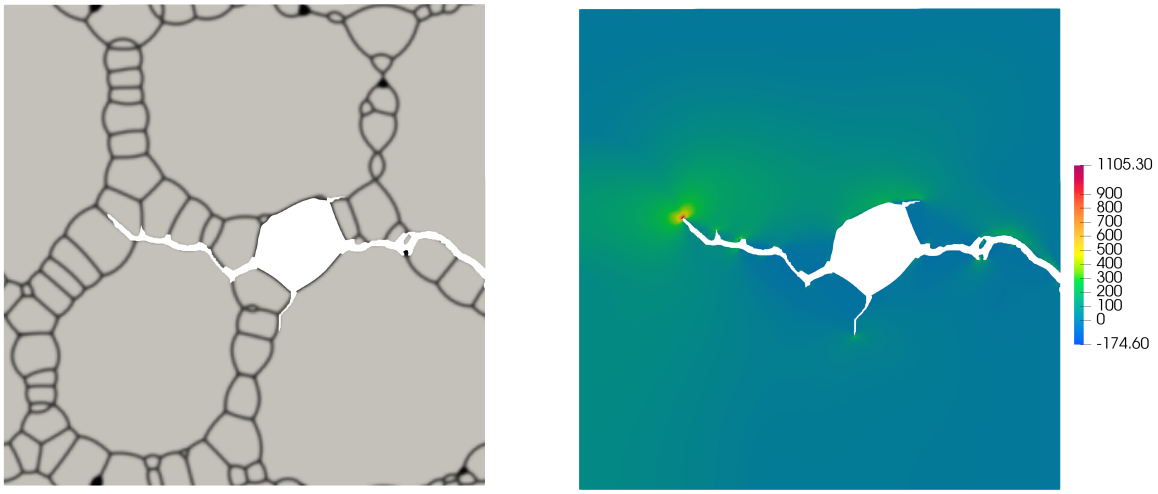

(a) (b)

Figure 23: 25 % recrystallization stage: (a) Crack propagation; (b) Maximum principal stress.

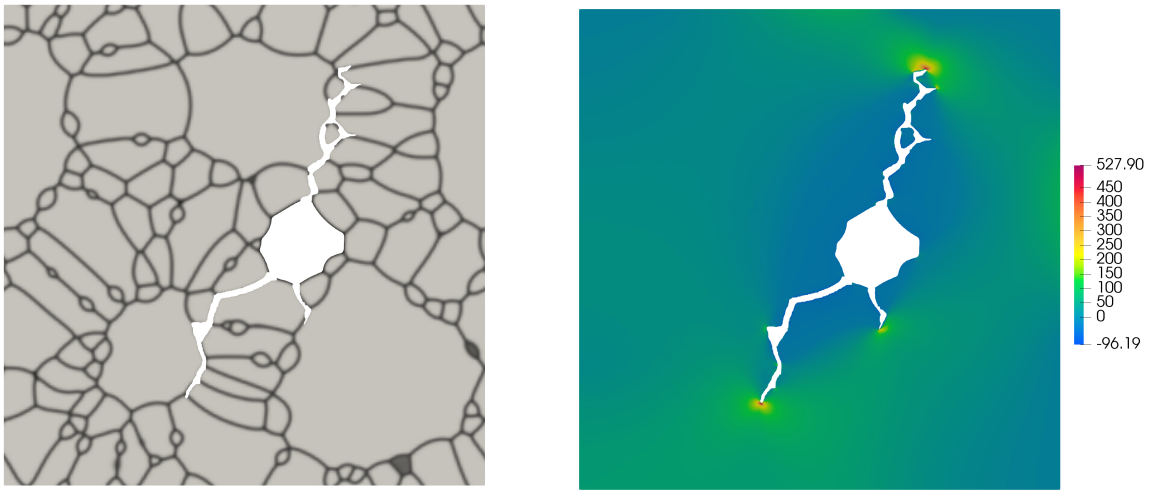

(a) (b)

Figure 24: 60 % recrystallization stage: (a) Crack propagation; (b) Maximum principal stress.

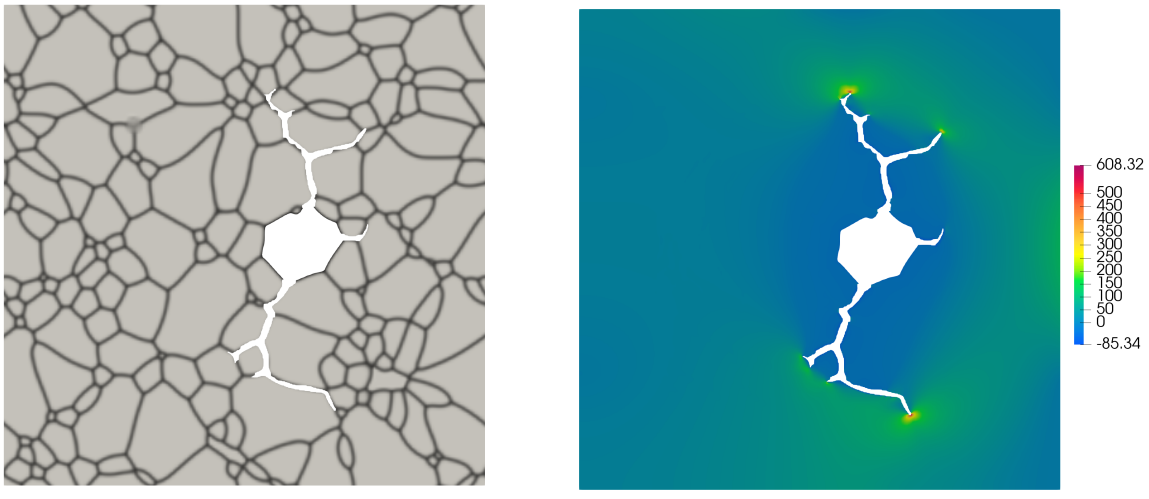

(a) (b)

Figure 25: 100 % recrystallization stage: (a) Crack propagation; (b) Maximum principal stress.

4.4 Pulverization Criterion Determination

The macro-scale pulverization behavior is approximated by using periodic boundary conditions (PBCs). PBCs are useful to avoid boundary effects caused by finite size and make the system deform like an infinite one. In MOOSE, the global strain system was implemented to enforce the PBC [63]. The global strain system is capable of capturing the deformation with applied loads while still maintaining the periodicity. A PBC example is shown in Figure 26, where the crack patterns are periodic and different sizes of fragments are observed.

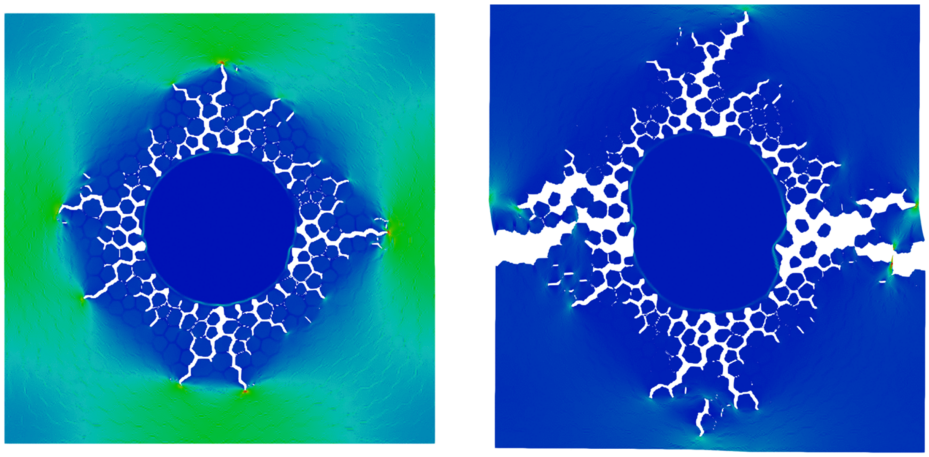

Figure 26: Crack propagation with PBC.

Our phase-field fracture models were used to develop a BISON pulverization criterion based on the bubble pressure. Pulverization occurs when the bubble pressure exceeds the critical value. The function of the critical bubble pressure is taken as

$$P_g^{cr} = [a + b(\sigma_{cr} - 130)](1 - p) - cP_{ext} \tag{82}$$

where σ_{cr}(MPa) is the critical fracture stress, p is the porosity, P_{ext}(MPa) is the external pressure, and a, b, and c are fitting coefficients. To determine those coefficients, we performed a series of simulations with different values of porosity, critical stress and external pressure. Figure 27 shows five initial configurations with different bubble distance ranging from 1.1 to 1.7 μ m. The porosity is calculated as $\pi r^2/(2l)^2$, where r is the bubble size of 0.5 μm and l is the bubble distance. The external pressures of 0 MPa, 30 MPa and 60 MPa are applied at all boundaries as shown in Figure 28. Due to uncertainty in determining the critical fracture stress for high-burnup UO_2 from macroscale data on porous samples, we consider three critical fracture stress of 130, 160 and 200 MPa. The pressure inside a bubble results in a circumferential tensile stress in the matrix. When this tensile stress reaches critical fracture strength, cracks will initiate at the bubble/matrix interface. The critical pressure values extracted from all simulations are provided in Tables 4, 5, and 6 for critical stress of 130 MPa, 160 MPa, and 200 MPa, respectively. The implementation in BISON of a function that is fit to this data is described in Section 5.

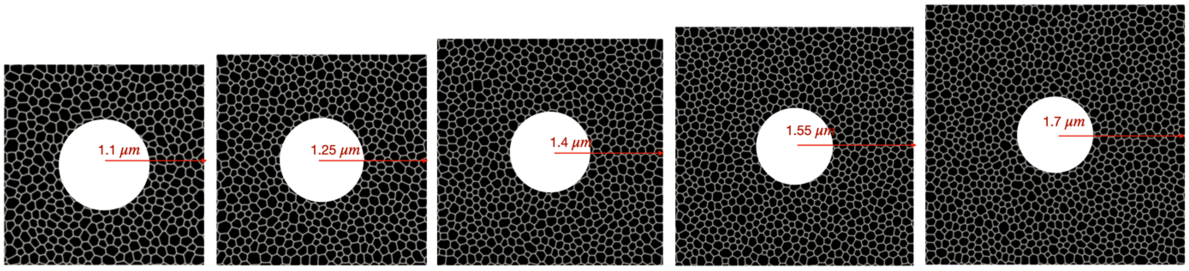

Figure 27: Initial configuration with different bubble distances.

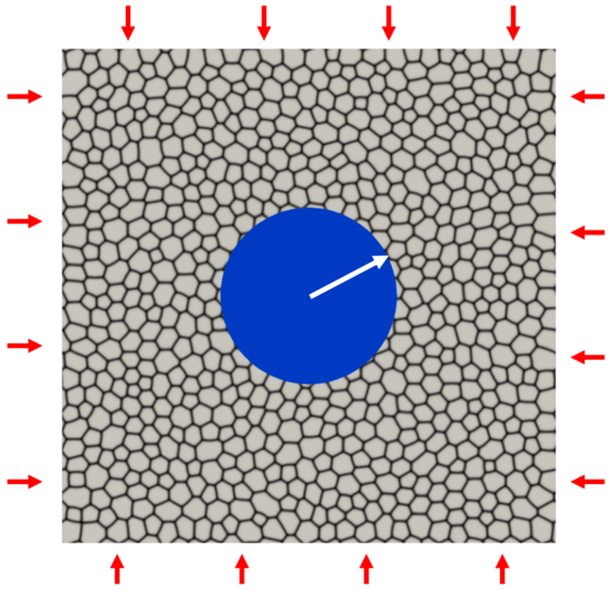

Figure 28: Periodic boundary conditions with external pressure loading.

Porosity / P_{ext}(MPa)	0.162	0.126	0.100	0.082	0.068
0	104	108	112	114	116
30	132	140	144	148	164
60	164	168	172	176	180

Table 4: Critical pressure values for $\sigma_{cr} = 130$ MPa.

Porosity / P_{ext}(MPa)	0.162	0.126	0.100	0.082	0.068
0	112	120	124	124	128
30	144	152	152	156	160
60	172	180	188	188	192

Table 5: Critical pressure values for $\sigma_{cr} = 160$ MPa.

Porosity / P_{ext}(MPa)	0.162	0.126	0.100	0.082	0.068
0	128	136	140	144	148
30	156	168	168	172	176
60	188	196	200	204	208

Table 6: Critical pressure values for $\sigma_{cr} = 200$ MPa.

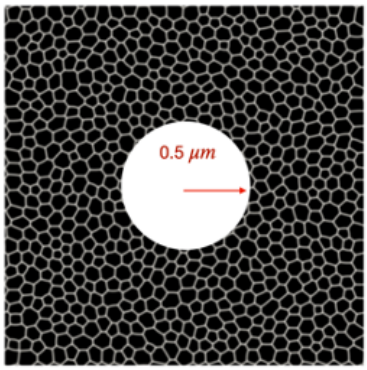

Figure 29: Geometry used to determine pulverization criteria for BISON using both analytical and phase-field fracture approaches. A 0.5 μm radius bubble is in the center of the simulation domain, surrounded by restructured grains with average grain radius 85 nm. Periodic boundary conditions are used.

5 BISON PULVERIZATION MODEL

5.1 Introduction

Based on the models and results described in this report, a mesoscale-based criterion for pulverization of high-burnup UO_2 fuel has been implemented in BISON. This has been implemented as a material property called `UO2PulverizationMesoscale`. Pulverization criteria based on both an analytical formulation and phase-field fracture simulation results are available. For both criteria, a simplified geometry of the HBS region is assumed, comprised of a single bubble surrounded by the smaller grains that result from HBS formation (see Figure 29). Periodic boundary conditions are used to enable this simulation domain to represent a periodic arrangement of these bubbles. This also allows the model to account for interactions between bubbles, the importance of which was discussed in Section 4.3.2, albeit in a limited way because it does not allow for variations in spacing between bubbles. The bubble radius used for both criteria was based on the most frequently observed bubble radius in experiments, 0.5 μm [64]. The domain size is varied while maintaining a constant bubble size to consider the effect of variation in porosity.

To determine whether pulverization occurs, the `UO2PulverizationMesoscale` material calculates the current pressure in the bubble P_g and compares it to the critical pressure for pulverization, P_g^{cr}. P_g^{cr} is determined based on either the analytical or phase-field fracture criterion, whichever is selected by the user. The details of these calculations are given in the following sections. Additionally, it is assumed that the local volume fraction of HBS formation must be greater than a threshold value in order for pulverization to occur. This value is currently assumed to be 50%, but future mesoscale simulations will be used to better quantify this threshold. If $P_g > P_g^{cr}$ and the local HBS volume fraction is greater than the threshold, pulverization is deemed to have occurred, and the material property `pulverized` is changed from 0 to 1.

5.2 Bubble Pressure Calculation

The `UO2PulverizationMesoscale` material calculates the current pressure in a representative 0.5 μm bubble based on a reference pressure P_0 and temperature T_0 at the onset of HBS formation. Based on the results of Section 2, a reference pressure of 123 MPa and temperature of 1200 K are suggested as an initial estimate; however, P_0 and T_0 are user-adjustable parameters to allow for future results to be incorporated easily into the model.

Based on the results of Section 3, it is assumed that during a LOCA transient, the size of the bubbles

does not change, so the density of gas within the bubbles is also unchanged. In that case, the current pressure in the bubble can be calculated using a relationship derived from the van der Waals equation of state as

$$P_g = \frac{P_0 T}{T_0} \tag{83}$$

5.3 Analytical Pulverization Criterion

The analytical criterion for pulverization is based on an expression that was originally developed for fragmentation along grain boundaries for lenticular bubbles in UO_2 [65]. Because pulverization is predominantly observed to occur in regions where the HBS in UO_2 fuel has formed, this model has been adapted to apply to the morphology of bubbles in the HBS region, which are approximately spherical. In this model, P_g^{cr} is given by:

$$P_g^{cr} = \frac{2\gamma}{r} + \frac{\sigma_{gb}^{cr}(1-\phi_2) - \sigma_H}{\phi_2} \tag{84}$$

where γ is the surface tension of the bubble-fuel interface, r is the bubble radius, σ_{gb}^{cr} is the critical fracture stress of the grain boundaries intersecting the bubble, ϕ_2 is areal fraction of the grain boundary occupied by the bubble, and σ_H is the local hydrostatic stress. In applying this equation, it is assumed that there is a uniform array of the statistically most likely bubbles, and that a flat grain boundary intersects each bubble; this neglects the more complex actual morphology of the bubbles and of the grain boundaries in the HBS. The fact that the actual grain boundaries are more complex and require the crack to change direction as it propagates may cause the analytical model to underestimate the actual stress required for fragmentation.

Given the assumed geometry, ϕ_2 can be calculated from the local porosity in the HBS structure, p, using

$$\phi_2 = \left(\frac{3p\sqrt{\pi}}{4}\right)^{2/3} \tag{85}$$

γ is given by $(0.85 - 1.4\times10^{-4}(T - 273.15))$ J/m^2, where T is in K [66]. σ_{gb}^{cr} is assumed to be 130 MPa [56].

5.4 Phase-field Fracture Simulation-based Pulverization Criterion

As described in Section 4, a function of the form

$$P_g^{cr} = [a + b(\sigma_{cr} - 130)](1-p) - cP_{ext} \tag{86}$$

was used for the pulverization criterion. The values of a, b and c are fit to the data in Section 4 using Python's `curve_fit` function. The fitted function of critical bubble pressure is given as

$$P_g^{cr} = [124.17 + 0.4386(\sigma_{cr} - 130)](1-p) + 1.018P_{ext} \tag{87}$$

where pressures and stresses are given in MPa. The fitted function and simulation data are plotted in Figure 30. A linear trend is observed for all the input parameters.

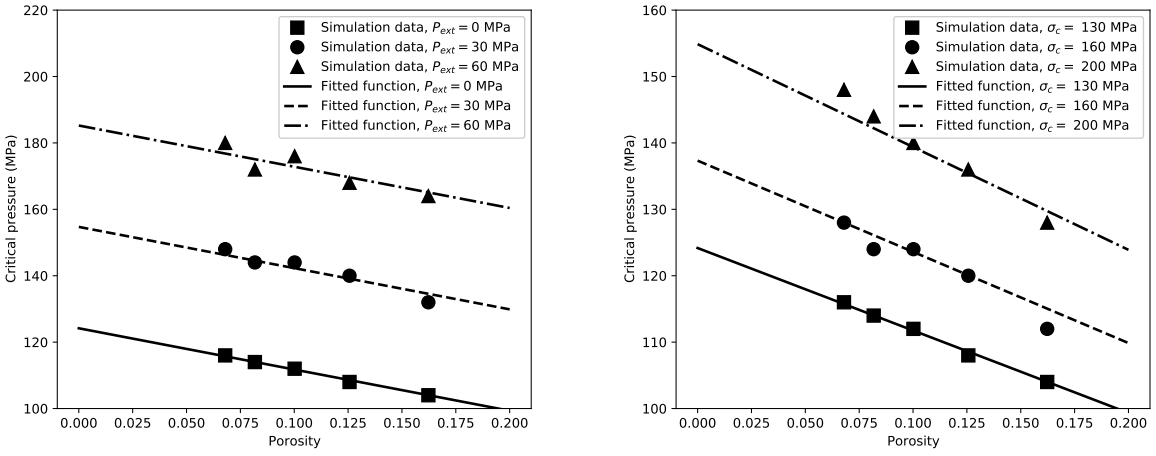

(a) (b)

Figure 30: Fitted function with: (a) different external pressure; (b) different critical fracture stress.

6 OVERALL CONCLUSIONS AND FUTURE WORK

In this work, mesoscale simulations have been used to develop and parameterize a mechanistic model for pulverization in BISON. The function used in fitting the phase-field fracture simulations appears to represent the data well. However, the model predictions of pulverization have yet to be used in integral BISON simulations of LOCA transients and compared to experiment using BISON validation cases. The critical step of applying the pulverization model in validation cases will be completed in a separate milestone by the end of FY-21.

In addition, the individual mesoscale models described in this report should be validated against experiments. Initial comparisons of the microstructures predicted by the model of Section 2 to experiments have been performed, and the results are encouraging; however, more quantitative assessment is needed. The pressure of gas bubbles in the HBS structure predicted by the models of both Section 2 and 3 should also be validated against experimental data. Currently, to our knowledge, no data is available on the pressure of bubbles in the HBS region; the need for such data has been communicated to experimental collaborators working in the Advanced Fuels Campaign (AFC) program.

Another pressing data need for improvement of the model is better estimates of $\mathcal{G}_c$ and σ_c for the phase-field fracture model. The current value of $\mathcal{G}_c$ used is an assumption only. The value of σ_c currently used is based on an extrapolation of data from porous large-scale samples back to zero porosity. Initial data from collaborators in the AFC program have suggested that σ_c could be much larger than the value currently used. In future work, atomistic and experimental work should provide improved estimates of these properties.

Finally, atomistic simulations have shown that additional defect species that are not included in the models here, such as interstitials, may have an important effect on the microstructural evolution. Additionally, clusters of defects may play an important role in transport because such clusters are energetically favorable to form, and the mobilities of such clusters may be significantly different from the individual defects that comprise them. Strategies to incorporate such defect clusters into the phase-field models will be developed in future work.

7 References

1. F. Pimentel and F. Smith. The economic benefits and challenges with utilizing increased enrichment and fuel burnup for light-water reactors. Technical report, Nuclear Energy Institute, 2019.

2. M. Helin and J. Flygare. NRC LOCA tests at Studsvik, design and construction of test train device and tests with unirradiated cladding material. Technical Report STUDSVIK/N-11/130, Studsvik, 2012.

3. M. Flanagan and P. Askeljung. Observations of fuel fragmentation, mobility and release in integral high-burnup, fueled loca tests. In *Enlarged Halden Program Group Meeting 2011*, 2011.

4. J. A. Turnbull, S. K. Yagnik, M. Hirai, D. M. Staicu, and C. T. Walker. An assessment of the fuel pulverization threshold during LOCA-type temperature transients. *Nuclear Science and Engineering*, 179:477–485, 2015.

5. V. V. Rondinella and T. Wiss. The high burn-up structure in nuclear fuel. *Materials Today*, 13:24–32, 2010.

6. K. Nogita and K. Une. Irradiation-induced recrystallization in high burnup UO_2 fuel. *Journal of Nuclear Materials*, 226(3):302–310, 1995.

7. K. Lassmann, C. T. Walker, J. van de Laar, and F. Lindström. Modelling the high burnup UO_2 structure in LWR fuel. *Journal of Nuclear Materials*, 226:1–8, 1995.

8. Y Zhang, D Schwen, L Aagesen, C Jiang, W Jiang, B Beeler, A Jokissari, S Biswas, S Novascone, S Andersson, and M Tonks. Marmot update for modeling light water reactor fuels. Technical Report INL/EXT-18-51592 Rev. 0, Idaho National Lab.(INL), Idaho Falls, ID (United States), 2018.

9. L. K. Aagesen, S. Biswas, W. Jiang, A. M. Jokisaari, D. Andersson, M. W. D. Cooper, and C. Matthews. Determine fragmentation criteria in high-burnup uo_2 fuel during accident conditions. Technical Report INL/EXT-20-00558, Idaho National Laboratory, 2020.

10. M. Plapp. Unified derivation of phase-field models for alloy solidification from a grand-potential functional. *Physical Review E*, 84(3):031601, 2011.

11. L. K. Aagesen, Y. Gao, D. Schwen, and K. Ahmed. Grand-potential-based phase-field model for multiple phases, grains, and chemical components. *Physical Review E*, 98:023309, 2018.

12. Ian Greenquist, Michael R. Tonks, Larry K. Aagesen, and Yongfeng Zhang. Development of a microstructural grand potential-based sintering model. *Computational Materials Science*, 172, 2020.

13. Ian Greenquist, Michael R. Tonks, Michael Cooper, David Andersson, and Yongfeng Zhang. Grand potential sintering simulations of doped uo2 accident-tolerant fuel concepts. *Journal of Nuclear Materials*, 532, 2020.

14. L. K. Aagesen, D. Schwen, M. R. Tonks, and Y. F. Zhang. Phase-field modeling of fission gas bubble growth on grain boundaries and triple junctions in UO_2 nuclear fuel. *Computational Materials Science*, 161:35–45, 2019.

15. Larry K. Aagesen, David Andersson, Benjamin W. Beeler, Michael W. D. Cooper, Kyle A. Gamble, Yinbin Miao, Giovanni Pastore, and Michael R.Tonks. Phase-field simulations of intergranular fission gas bubble behavior in u3si2 nuclear fuel. *Journal of Nuclear Materials*, 541, 2020.

16. D.R.Olander. *Fundamental aspects of nuclear reactor fuel elements*. Technical Information Center, Office of Public Affairs Energy Research and Development Administration, 1976.

17. C. Kittel and H. Kroemer. *Thermal Physics*. W. H. Freeman and Company, 1980.

18. D. Davies and G. Long. The emission of xenon-133 from lightly irradiated uranium dioxide spheroids and powders. Technical Report AERE-R 4347, Atomic Energy Research Establishment, 1963.

19. J. A. Turnbull, C. A. Friskney, J. R. Findlay, F. A. Johnson, and A. J. Walter. The diffusion coefficients of gaseous and volatile species during the irradiation of uranium dioxide. *Journal of Nuclear Materials*, 107:168–184, 1982.

20. C Matthews, R. Perriot, M. W. D. Cooper, C. R. Stanek, and D. A. Andersson. Cluster dynamics simulation of xenon diffusion during irradiation in UO_2. *Journal of Nuclear Materials*, in press:152326, 2020.

21. J. Spino, J. Rest, W. Goll, and C. T. Walker. Matrix swelling rate and cavity volume balance of UO_2 fuels at high burn-up. *Journal of Nuclear Materials*, 346:131–144, 2005.

22. Hj Matzke. Radiation enhanced diffusion in UO2 and (U, Pu)O2. *Radiation Effects*, 75(1-4):317–325, January 1983.

23. Hj Matzke. Atomic transport properties in u02and mixed oxides (u,pu)o2. *J. Checm Soc.*, 83:1121–1142, 1987.

24. N. Moelans, B. Blanpain, and P. Wollants. Quantitative analysis of grain boundary properties in a generalized phase field model for grain growth in anisotropic systems. *Phys. Rev. B*, 78:024113, 2008.

25. JB Ainscough, BW Oldfield, and JO Ware. Isothermal grain growth kinetics in sintered UO_2 pellets. *Journal of Nuclear Materials*, 49(2):117–128, 1973.

26. M. Idiri, T. Le Bihan, S. Heathman, and J. Rebizant. Behavior of actinide dioxides under pressure: UO_2 and ThO_2. *Physical Review B*, 70(1), 2004.

27. J. B. Wachtman, M. L. Wheat, H. J. Anderson, and J. L. Bates. Elastic constants of single crystal UO_2 at 25 degrees C. *Journal of Nuclear Materials*, 16(1):39–41, 1965.

28. D.A. Knoll and D.E. Keyes. Jacobian-free newton-krylov methods: a survey of approaches and applications. *J. Comput. Phys.*, 193:357–397, 2004.

29. Benjamin S. Kirk, John W. Peterson, Roy H. Stogner, and Graham F. Carey. libMesh: a C++ library for parallel adaptive mesh refinement/coarsening simulations. *Engineering with Computers*, 22:237–254, 2006.

30. Fabiola Cappia, David Frazer, Kaustubh Bawane, and Fei Teng. Local fracture strength and microstructure of high burnup uo2 fuel. Technical report, Idaho National Lab.(INL), Idaho Falls, ID (United States), 2020.

31. S. G. Kim, W. T. Kim, and T. Suzuki. Phase-field model for binary alloys. *Physical Review E*, 60(6):7186–7197, 1999.

32. Shenyang Hu, Charles H. Jr., Howard L. Heinisch, Marius Stan, Michael I. Baskes, and Steven M. Valone. Phase-field modeling of gas bubbles and thermal conductivity evolution in nuclear fuels. *Journal of Nuclear Materials*, 392(2):292 – 300, 2009.

33. Paul C. Millett and Michael Tonks. Meso-scale modeling of the influence of intergranular gas bubbles on effective thermal conductivity. *Journal of Nuclear Materials*, 412(3):281 – 286, 2011.

34. P. C. Millett, M. R. Tonks, and S. B. Biner. Grain boundary percolation modeling of fission gas release in oxide fuels. *Journal of Nuclear Materials*, 424(1-3):176–182, 2012.

35. Yulan Li, Shenyang Hu, Robert Montgomery, Fei Gao, and Xin Sun. Phase-field simulations of intragranular fission gas bubble evolution in UO_2 under post-irradiation thermal annealing. *Nuclear Instruments and Methods in Physics Research Section B: Beam Interactions with Materials and Atoms*, 303:62–67, 2013.

36. M. J. Welland, E. Tenuta, and A. A. Prudil. Linearization-based method for solving a multicomponent diffusion phase-field model with arbitrary solution thermodynamics. *Physical Review E*, 95:063312, 2017.

37. Z. Xiao, Y. Wang, S. Hu, Y. Li, and S.-Q. Shi. A quantitative phase-field model of gas bubble evolution in UO_2. *Computational Materials Science*, 184:109867, 2020.

38. V. I. Levitas and K. Samani. Size and mechanics effects in surface-induced melting of nanoparticles. *Nature Communications*, 2:284, 2011.

39. C Matthews, R. Perriot, M. W. D. Cooper, C. R. Stanek, and D. A. Andersson. Cluster dynamics simulation of uranium self-diffusion during irradiation in UO_2. *Journal of Nuclear Materials*, 527:151787, 2019.

40. D. A. Andersson, B. P. Uberuaga, P. V. Nerikar, C. Unal, and C. R. Stanek. U and Xe transport in $UO_{2\pm x}$: Density functional theory calculations. *Physical Review B*, 84:054105, 2011.

41. A. Durga, P. Wollants, and N. Moelans. Evaluation of interfacial excess contributions in different phase-field models for elastically inhomogeneous systems. *Modelling and Simulation in Materials Science and Engineering*, 21(5), 2013.

42. L. K. Aagesen, D. Schwen, K. Ahmed, and M. R. Tonks. Quantifying elastic energy effects on interfacial energy in the Kim-Kim-Suzuki phase-field model with different interpolation schemes. *Computational Materials Science*, 140:10–21, 2017.

43. R. Perriot, C. Matthews, M. W. D. Cooper, B. P. Uberuaga, C. R. Stanek, and D. A. Andersson. Atomistic modeling of out-of-pile xenon diffusion by vacancy clusters in UO_2. *Journal of Nuclear Materials*, 520:96–109, 2019.

44. A. Goyal, S. R. Phillpot, G. Subramanian, D. A. Andersson, C. R. Stanek, and B. P. Uberuaga. Impact of homogeneous strain on uranium vacancy diffusion in uranium dioxide. *Physical Review B*, 91:094103, 2015.

45. A. Goyal, K. Mathew, R. G. Hennig, A. Chernatynskiy, C. R. Stanek, S. T. Murphy, D. A. Andersson, S. R. Phillpot, and B. P. Uberuaga. The conundrum of relaxation volumes in first-principles calculations of charged defects in UO_2. *Applied Sciences*, 9:5276, 2019.

46. Y. Zhang, D. Schwen, P. Chakaraborty, C. Jiang, L. Aagesen, K. Ahmed, W. Jiang, B. Biner, X. Bai, M. Tonks, and P. Millett. Marmot update for oxide fuel modeling. Report INL/EXT-16-40039, Idaho National Laboratory, 2016.

47. International Atomic Energy Agency. Chain fission yields. https://www-nds.iaea.org/sgnucdat/c1.htm; accessed 13-Apr-2017.

48. B. Dorado, D. A. Andersson, C. R. Stanek, M. Bertolus, B. P. Uberuaga, G. Martin, M. Freyss, and P. Garcia. First-principles calculations of uranium diffusion in uranium dioxide. *Physical Review B*, 6(3):035110, 2012.

49. Cody J. Permann, Derek R. Gaston, David Andrš, Robert W. Carlsen, Fande Kong, Alexander D. Lindsay, Jason M. Miller, John W. Peterson, Andrew E. Slaughter, Roy H. Stogner, and Richard C. Martineau. MOOSE: Enabling massively parallel multiphysics simulation. *SoftwareX*, 11:100430, Jan.–Jun. 2020.

50. J. D. Hales, K. A. Gamble, B. W. Spencer, S. R. Novascone, G. Pastore, W. Liu, D. S. Stafford, R. L. Williamson, D. M. Perez, and R. J. Gardner. BISON users manual. Technical Report INL/MIS-13-30307, Rev. 3, Idaho National Laboratory, September 2015.

51. R. Bullough and R. C. Perrin. Growth, stability, and interactions of voids and gas bubbles in solids. In *Radiation Damage in Reactor Materials*, volume 2, pages 233–251. International Atomic Energy Agency, 1969.

52. D.A. Porter and K.E. Easterling. *Phase Transformations in Metals and Alloys*. Chapman and Hall, London, 2nd edition, 1992.

53. Zachary A. Wilson and Chad M. Landis. Phase-field modeling of hydraulic fracture. *Journal of the Mechanics and Physics of Solids*, 96:264 – 290, 2016.

54. Keita Yoshioka, Dmitri Naumov, and Olaf Kolditz. On crack opening computation in variational phase-field models for fracture. *Computer Methods in Applied Mechanics and Engineering*, 369:113210, 2020.

55. B. Bourdin, G.A. Francfort, and JJ Marigo. The variational approach to fracture. *Journal of Elasticity*, 91:5 – 148, 2008.

56. M. Oguma. Microstructure effects on fracture strength of UO_2 fuel pellets. *Journal of Nuclear Science and Technology*, 19:1005–1014, 1982.

57. Wen Jiang, Tianchen Hu, Larry K. Aagesen, and Yongfeng Zhang. Three-dimensional phase-field modeling of porosity dependent intergranular fracture in uo2. *Computational Materials Science*, 171:109269, 2020.

58. K. Govers. Comparison of interatomic potentials for UO_2. *Journal of Nuclear Materials*, 366:161–177, 2007.

59. C. Miehe, F. Welschinger, and M. Hofacker. Thermodynamically consistent phase-field models of fracture: Variational principles and multi-field FE implementations. *International Journal for Numerical Methods in Engineering*, 83:1273–1311, 2010.

60. C. Miehe, M. Hofacker, and F. Welschinger. A phase field model for rate-independent crack propagation: Robust algorithmic implementation based on operator splits. *Computer Methods in Applied Mechanics and Engineering*, 199:2765–2778, 2010.

61. R. L. Williamson, J. D. Hales, S. R. Novascone, G. Pastore, K. A. Gamble, B. W. Spencer, W. Jiang, S. A. Pitts, A. Casagranda, D. Schwen, A. X. Zabriskie, A. Toptan, R. Gardner, C. Matthews, W. Liu, , and H. Chen. Bison: A flexible code for advanced simulation of the performance of multiple nuclear fuel forms. *Nuclear Technology*, 2020.

62. Anders Puranen. Post test examinations on loca tested rods. Studsvik Report STUDSVIK/N-13/198, Studsvik, 2013.

63. Sudipta Biswas, daniel Schwen, and Jason D. Hales. Development of a finite element based strain periodicity implementation method. *Finite Elements in Analysis and Design*, 179, 2020.

64. K. Kulacsy. Mechanistic model for the fragmentation of the high-burnup structure during LOCA. *Journal of Nuclear Materials*, 466:409–416, 2015.

65. D. R. Olander. RIA-related issues concerning fission gas in irradiated PWR fuel. Technical report, Institut de Protection et de Surete Nucleaire, Cadarache, France, 1997.

66. R. O. A. Hall, M. J. Mortimer, and D. A. Mortimer. Surface energy measurements on UO_2 - a critical review. *Journal of Nuclear Materials*, 148:237–256, 1987.